Controlling and Probing Polaritons in the Mid- to Far-Infrared

T. G. Folland[1], L. Nordin[2], D. Wasserman[2], and J. D. Caldwell[1]

[1]Department of Mechanical Engineering, Vanderbilt University, TN, 37212, USA

[2]Department of Electrical and Computer Engineering, University of Texas at Austin, Austin, TX, 78758, USA

ABSTRACT

The long free-space wavelengths associated with the mid- to far-infrared spectral range impose significant limitations on the form-factor of associated optic and electro-optic components. Specifically, current commercial optical sources, waveguides, optical components (lenses, waveplates) and detector elements are larger than the corresponding diffraction limit, resulting in reduced image resolution and bulky optical systems, with deleterious effects for a number of imaging and sensing applications of interest to commercial, medical and defense related arenas. The field of nanophotonics, where the ultimate objective is to confine and manipulate light at deeply sub-wavelength, nanometer length-scales, offers significant opportunities to overcome these limitations. The demonstration of nano-scale optics at the many-micron scale in the infrared can be achieved by leveraging polaritons, quasi-particles comprised of oscillating charges within a material coupled to electromagnetic excitation. However, the predominant polaritonic materials and the characterization techniques and methods implemented for measuring these quasiparticles in the mid- to far-IR require a different approach with respect to similar efforts in the ultraviolet, visible and near-IR. The purpose of this tutorial article is to offer an overview of the basic materials, tools and techniques for exciting, manipulating, and probing polaritons in the mid- to far-infrared wavelength range, providing a general guide to sub-wavelength, and sometimes nano-scale optics for those entering this exciting and burgeoning research field.

I. INTRODUCTION

Polaritons are quasi-particles that consist of light coupled to coherently oscillating charges in a material. A broad range of different types of polaritons exist,[11] with arguably the most well-studied being surface plasmon polaritons (SPPs). These quasiparticles are surface waves where the oscillating charge that couples to the electromagnetic wave are free carriers within a conductive material, resulting in the formation of an evanescent wave that propagates along the interface between the conductor and the dielectric environment (e.g. metal film in air).[12] The frequency range across which SPPs can be supported by a given metal/dielectric interface is determined by the plasma frequency (ω_p) of the carriers (electrons or holes) in the conductor – essentially how rapidly electrons/holes can respond to an incident electromagnetic field – and the permittivity of the dielectric material. In noble metals (e.g. Ag, Au), ω_p is in the ultraviolet or visible range due to the high free-carrier concentrations of metals, and thus, SPPs are predominantly observed in the shorter wavelength visible and near-infrared (NIR) spectral ranges. The main advantage of SPPs over traditional dielectric materials is found in their ability to dramatically compress the free-space wavelength at a given frequency. This allows for the confinement of optical frequency electromagnetic fields to spatial volumes well below the diffraction limit, which in turn provides a method for realizing significant reductions in the size and form-factor of optical components.[13] In addition SPPs offer mechanisms for strengthening light-matter interactions for enhanced chemical sensing,[9,14,15] modifying the radiative recombination rates of emitters[16] or enhanced radiative heat transfer rates.[17] However, one major limitation of noble-metal SPPs in the visible is the high material absorption inside the metal when the electromagnetic field becomes confined.[18] This has prevented visible SPP modes from being used to replace traditional diffraction-limited dielectric waveguides and/or cavities with polariton-supporting optical structures, as existing technologies are often superior. However, optical loss can also be an advantage,[19,20] as absorption results in power dissipation and an associated local temperature increase, which has provided significant advantages in strongly localized (subwavelength) heat sources.[6,21,22] As a result, many of the most promising potential applications for plasmonic structures at these wavelengths, such as heat-assisted magnetic recording (HAMR),[23] photothermal cancer therapy,[24] and nanoparticle assisted solar vapor generation,[25] all leverage the ability of plasmonic nanoparticles to absorb light and thus heat their local environment. In effect, such structures act as transducers, efficiently converting optical to thermal energy, with the added advantage of providing highly localized heating.

The limitations of SPPs in replacing diffraction-limited optical components in the visible motivates the study of polaritonic phenomena in different spectral windows, where technologies are less developed, and thus the requirements for component properties are somewhat more relaxed. The mid- (MIR) to far-infrared (FIR) provide a natural choice for the study of polaritons for numerous reasons. First, a broader range of materials support SPPs in the IR, including doped commercial semiconductors, 2D materials, intermetallics, and semiconducting oxides.

In addition to SPP modes, this spectral range also offers the ability to realize surface phonon polaritons (SPhPs), which form at the surface of polar dielectrics.[26,27] These alternative polaritons arise from the interaction of light with polar optic phonons and have inherently longer scattering lifetimes than SPPs, resulting in lower optical losses.[27,28] The confinement of IR light to dimensions below the diffraction limit with SPPs and/or SPhPs has significant implications for IR devices, as the long free-space wavelengths reduce the strength of interactions with matter and the achievable optical component sizes in traditional approaches. Furthermore, unlike in noble metals, the number of charge carriers in semiconductors can be controlled, hence providing the opportunity to dictate the SPP frequency, using either dopants[29,30] or carrier excitation,[31-33] making them tunable spectrally, and offering schemes towards optical modulation.[34] Infrared polaritons are therefore highly versatile, with the potential to significantly advance the current state-of-the-art in IR optics, including IR modulators, light sources, polarizers and detectors. One of the major challenges in realizing IR-polariton-based devices is finding the appropriate materials, tools and experimental designs for these investigations. In contrast to visible wavelengths, where glass-based objectives, optics and spectrometers are ubiquitous, compact and highly efficient, the techniques for studying IR optical properties, and specifically IR polaritons, are generally less widely used and understood. This tutorial is designed to introduce the general concepts associated with IR polaritonics, specifically addressing the basic underlying physical mechanisms of the origin of the predominant polariton types, how they can be stimulated, the measurement approaches required for such investigations, and how these efforts are modified when transitioning from the MIR to FIR. Finally, we provide examples of how various IR polaritons have been studied to illustrate the concepts discussed. It is our hope that this tutorial will provide a complete introduction to better prepare scientists and engineers to the expanding field of IR nanophotonics and metamaterials and aid in shortening the learning curve for those applying these concepts for realizing advanced IR technologies.

II. INFRARED POLARITONS

Polaritons are quasiparticles that form when light strongly couples to coherently oscillating charges in a material. They can exist both within the bulk of a material (volume polaritons) or alternatively on the surface of the material (surface polaritons). Volume polaritons occur when the dielectric function of the polaritonic medium is positive and the charges oscillate coherently with the incident electromagnetic wave (examples including phonon polaritons, plasmon polaritons and intersubband polaritons[35]). However, as introduced above, for this tutorial we are focused on the class of surface polaritons, which are supported at the interface between a metallic-like material (negative real part of the dielectric permittivity) and a dielectric (positive real permittivity). It is this class of polaritons that enables the confinement of light on length-scales below the diffraction limit due to the formation of an evanescent wave at the interface between the two materials. Overcoming the diffraction limit has significant implications for IR optics, providing a path towards enhancing the interaction of IR light featuring long free-space wavelengths to deeply sub-wavelength scale structures, devices and materials.[5] Negative permittivity is a direct consequence of the
3

coherently oscillating charges in a material, which induce a surface screening field, causing a high reflection of the incident optical field, and hence prevent propagation into the bulk. In the IR, negative permittivity is commonly realized in materials with excess free charge carriers and/or polar optic phonons. We highlight that other processes, such as strong intersubband absorption and exciton formation, can also produce negative permittivity, however these are outside the scope of this tutorial, and are covered elsewhere.[11,36]

We will now address how IR SPPs and SPhPs form, their characteristic properties and the mechanisms by which they can be excited. For SPPs the negative permittivity is a result of free charge carriers, which produce a local screening field that occurs when electrons with density n are stimulated to move coherently with an incident electric field[12]. Mathematically, this can be well-defined by the Drude formalism, which takes the functional form:

$$\varepsilon(\omega) = \varepsilon_\infty \left(1 - \frac{\omega_p^2}{\omega^2 - i\gamma\omega}\right) \qquad (1)$$

where ω_p is the the plasma frequency, and is defined by $\omega_p = \sqrt{ne^2/\varepsilon_0\varepsilon_\infty m_e}$ (n is the carrier concentration, m_e is the electron mass, e is the electronic charge), ε_∞ is the high frequency dielectric constant, and γ represents the free carrier damping. The plasma frequency sets the upper limit in frequency where the free carriers in that material can coherently respond to the incident radiation and effectively screen it out. At the high carrier concentrations of metals (n~10^{23}cm^{-3}), the ω_p will occur within the visible or UV, and thus these materials form the basis of visible plasmonics.[12] To support SPP modes in the IR we can instead use heavily doped semiconductors. A major advantage of SPPs in doped semiconductors is found in the ability to dictate and potentially modulate the carrier density through intentional doping[4,29,37,38], electrostatic gating [39-41] or optical pumping[32,33,42]. This means that the dielectric function can be potentially tuned over a broad range of frequencies throughout the IR during the growth process or dynamically modified using external stimuli.

Surface phonon polaritons, while similar in many ways to the previously described SPPs, offer a significant suite of novel properties that are desired for a range of potential IR applications. All crystalline materials support phonons (coherent vibrations of the atomic lattice), of which certain classes interact with light. Here we are interested in optic phonons, as these oscillate at frequencies commensurate with light in the mid- to far-IR. Optic phonons exist as transverse (transverse optic; TO) or longitudinal (longitudinal optic; LO) displacement waves. The frequencies of these phonons (ω_{TO}, ω_{LO}) are determined by the crystal lattice structure, the constituent atomic masses, bond strength and transverse effective charge.[27,43] For non-polar bonds (e.g. Si or Ge) the TO and LO phonons are degenerate in energy at the Γ point (center of the Brillouin zone), however, the difference in electronegativities across a diatomic bond (e.g. SiC) results in a net dipole moment, causing a spectral splitting of the LO phonon to higher energies with respect to the TO.[43] The corresponding net dipole moment of the TO phonon in turn makes it IR active, allowing this net charge to induce a surface screening field. Thus, analogous to free carriers in a metal or highly doped semiconductor, the coherently oscillating ionic lattice charges induce a high reflectivity within a

4

defined spectral range. This spectral window is referred to as the 'Reststrahlen band', and is spectrally located between TO and LO phonon energies.[43,44] Correspondingly, this will result in the real part of the permittivity becoming negative, mathematically expressed using the well-known "TOLO" formalism:

$$\varepsilon(\omega) = \varepsilon_\infty \left(1 + \frac{\omega_{LO}^2 - \omega_{TO}^2}{\omega_{TO}^2 - \omega^2 - i\omega\Gamma} \right) \qquad (2)$$

Similar to electrons, each phonon mode has a characteristic scattering time τ, and an corresponding damping constant Γ, for full details see Ref 45. This region of negative permittivity is where SPhP modes can be supported. Two important distinctions between the free carrier plasma and polar phonons is the increased scattering lifetime of the phonon oscillations and the significantly larger spectral dispersion of the permittivity for polar crystals. In the case of the former, the scattering lifetime of phonons is generally on the order of picoseconds[27] (vs tens to hundreds of femtoseconds for the scattering of free carriers),[46] significantly reducing losses associated with SPhPs. Indeed, recently phonon lifetimes within MoO_3 were reported upwards of 20 ps.[47] This increased phonon lifetime has been demonstrated to have an equivalent increase in the lifetime of resulting polaritons.[2,20,48,49] However, the large spectral dispersion within the Reststrahlen band of polar materials results in a very slow group velocity, and thus an extremely slow light.[27,47,50]

The surface polariton is a direct solution of Maxwell's equations,[12] and is characterized by the evanescent decay of the electromagnetic fields from the surface of the polaritonic medium both into that medium and the adjacent dielectric, along with propagation of the fields along the interface with the wavevector ($k_{sp} = 2\pi/\lambda_{sp}$), where λ_{sp} represents the compressed wavelength of the surface polariton. The relationship between k and the dielectric function at the two boundaries is provided by the phonon polariton dispersion expression:

$$k = k_0 \sqrt{\frac{\varepsilon_m \varepsilon_d}{\varepsilon_m + \varepsilon_d}} \qquad (3)$$

where ε_m and ε_d are the relative permittivity of the polaritonic and dielectric materials, respectively, and k_0 represents the free-space wavevector of the incident light ($k_0 = 2\pi/\lambda_0$). This function is plotted in Fig. 1a for a polar crystal, highlighting the dispersion of the bulk volume phonon polaritons at frequencies above and below the Reststrahlen band (gray curves), with the SPhP dispersion found within this band (black curve). Here we have assumed a lossless (γ=0) polar dielectric material and vacuum as the dielectric environment. Note that as the real part of the permittivity in the material approaches $Re(\varepsilon_m) = -Re(\varepsilon_d)$, k asymptotically approaches infinitely large values. As k is inversely proportional to λ, this implies λ_{sp} becomes infinitely small, and thus, at this point the light can become confined to essentially arbitrarily small sizes in a loss-less medium. While the form plotted in Fig. 1a assumes a TOLO dielectric function, a similar dispersion curve is observed for any polaritonic material. While the relation in Eq. (3) describes the properties of a surface polariton propagating on an infinitely thick polaritonic medium, polaritons can also be supported in extremely thin films (<λ/100). In such systems, polaritons can form on both interfaces of the film, but due to the reduced thickness, the two modes may couple resulting in a

5

close to non-dispersive, highly absorbing mode at a fixed frequency near ω_p or ω_{LO}, where the permittivity crosses zero.[51-55] This epsilon near zero (ENZ) polariton mode[56] exhibits a reduced linewidth with respect to the surface polariton modes, and provides an extremely efficient light absorber, which is discussed at greater length in Refs. [51,54,57-59].

The challenge associated with both studying and using surface polaritons is that they propagate much slower than free-space electromagnetic radiation. Thus, due to the requirement to conserve both energy and momentum, it is impossible to directly excite surface polaritons with regular plane waves (which lie on the light line, red line in Fig. 1a). This 'momentum mismatch' between plane waves and polaritons can be overcome by slowing down the incident light using a range of techniques. One of the easiest methods incorporates prism coupling (shown in Fig. 1b and c).[8,60] Prism coupling exploits the evanescent wave that results at the boundary of a high refractive index prism, either in contact with (Fig. 1b) or close to the polaritonic medium (Fig. 1c), with these two approaches
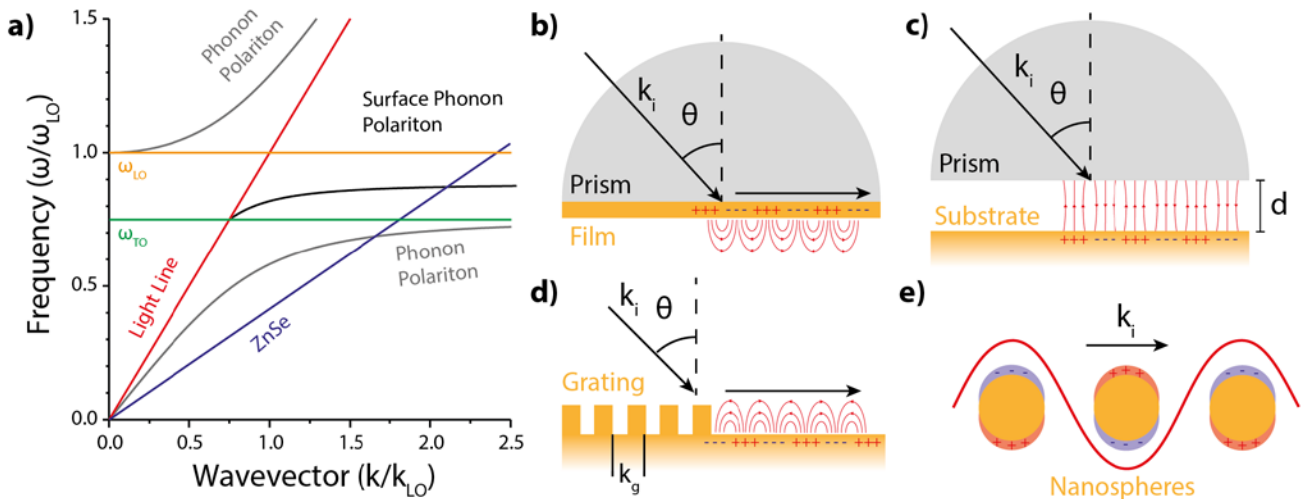

Figure 1: Surface Polariton dispersion and coupling, adapted from [5]. a) The dispersion relationship for electromagnetic waves in a polar semiconductor, highlighting the region between ω_{TO} and ω_{LO} which supports surface phonon polaritons. b)-e) Due to the momentum mismatch between free space light and polaritons, methods to probe them require this mismatch to be overcome. This can be realized by coupling light to the polaritonic medium through a high index prism in either the b) Kretschmann or c) Otto configurations, by d) imparting higher momentum through grating coupling or e) through nanostructuring of the polaritonic medium, resulting in sub-diffractional resonant cavities.

referred to as the Kretschmann and Otto configurations, respectively. This allows coupling into polaritons with $k_{sp} = n_{prism} sin(\theta) k_0$, where θ is the incident angle (blue line for light line in ZnSe in Fig. 1a). A second route is through exploiting diffraction gratings, where additional momenta is provided by the periodicity of the grating (Fig. 1d). This is essentially a form of Bragg scattering - light interacts with the grating, causing it to be slowed due to coupling into diffractive modes. In all of these approaches by changing the angle of incidence θ, the momentum at a given incident frequency can be tuned to match the momentum offset between free-space light and the polariton mode (See Fig. 1a). The final method of exciting surface polaritons is by coupling free-space light to sub-

wavelength particles (Fig. 1e), where the additional momentum is provided by Mie scattering from the small particle size.[26] This is visualized for spherical particles in Fig. 1e, but is generally observed in a range of resonant nanoparticle geometries fabricated via top-down[3,61,62] or bottom-up approaches.[63] Note that in this case we are generally exciting localized polaritons, as opposed to the propagating modes excited via prism or grating coupling. The result is the formation of a resonant antenna that can be deeply subdiffractional in scale, with the resonant frequency determined by the shape and size of the structure. Therefore, by plotting the resonant frequency as a function of nanoparticle size and/or shape, the surface polariton dispersion can again be extracted, analogous to Fig. 1a. Nanoparticle scattering is also the methodology behind the stimulation of polaritons within the near-field optical microscopy techniques, which will be covered later in this paper. While the above description describes any polaritonic system (including those in both visible and infrared), the IR poses a unique set of challenges when compared to the near-IR or visible including the longer free-space wavelengths, associated window materials, detectors and sources.

The remainder of this tutorial article will introduce the appropriate measurement techniques, beginning with Fourier transform infrared (FTIR) spectroscopy, the predominant method for collecting spectra from the MIR to FIR. We will then highlight methods for measuring spectra from smaller regions of interest including FTIR microscope operation and nano-FTIR and scanning optical probe techniques. We follow this by discussing the additional challenges associated with such measurements in the FIR. Building upon this introduction, we then provide a few key examples where some of these techniques have been implemented previously in the literature.

III. MEASUREMENT TECHNIQUES

Fourier Transform Infrared (FTIR) Spectroscopy of Polaritons in the Mid-IR

All methods of exciting surface polaritons result in resonant reflection (R), transmission (T), absorption (A) and/or scattering (S) of electromagnetic waves incident on the polaritonic medium, (where R+T+A+S=100%). For full characterization of the polariton modes, the frequency and linewidth must be measured, requiring appropriate IR spectroscopic techniques. The primary tool for such measurements in the IR is the FTIR spectrometer. While FTIR has historically been used to understand chemical compounds, it also provides a versatile platform for measurements of solid-state samples, including polaritonic materials, structures and devices. However, FTIR is based upon different operational principles, components and techniques than the dispersive spectrometers typically used in the UV-visible-NIR spectral ranges. This section will outline the operation and specific techniques relevant for measuring polaritons via FTIR spectroscopy.

In brief, a FTIR spectrometer consists of a broad-band IR source (typically a SiC glowbar), a Michelson interferometer, a sample compartment, and an IR detector (see Fig. 2a). The optical power transmitted through the

sample compartment is measured by the detector as a function of the position of a moving mirror, forming an interferogram, which is the Fourier transform (FT) of the IR spectrum. A discrete FT is then performed on the interferogram, extracting the spectrally dependent IR signal passing through the spectrometer. This approach to optical spectroscopy has several advantages over dispersive spectroscopic techniques. First, the measurement is inherently broadband, appropriate for measurements from >1000 µm to approximately 1 µm (depending on the performance of the source, beam splitter and detector). Second, as all frequencies are collected simultaneously, there is no trade-off between spectral resolution and signal strength, generally resulting in high signal-to-noise. Finally, the spectral resolution is determined by the interferometer path length, which can be extremely large, with commercial models available with sub-GHz frequency resolution. However, there are also several complications of FTIR spectroscopy. Some of the most significant challenges arise from the process of converting an interferogram into a spectrum. Signal processing techniques are applied in the process of creating the spectrum (notably phase correction, apodization and zero filling[64]), which can influence the interpretation of the results if applied incorrectly. Furthermore, detector nonlinearities induce significant spectral distortion into the FT process, and as such any experiment must be carefully designed to achieve reliable results.
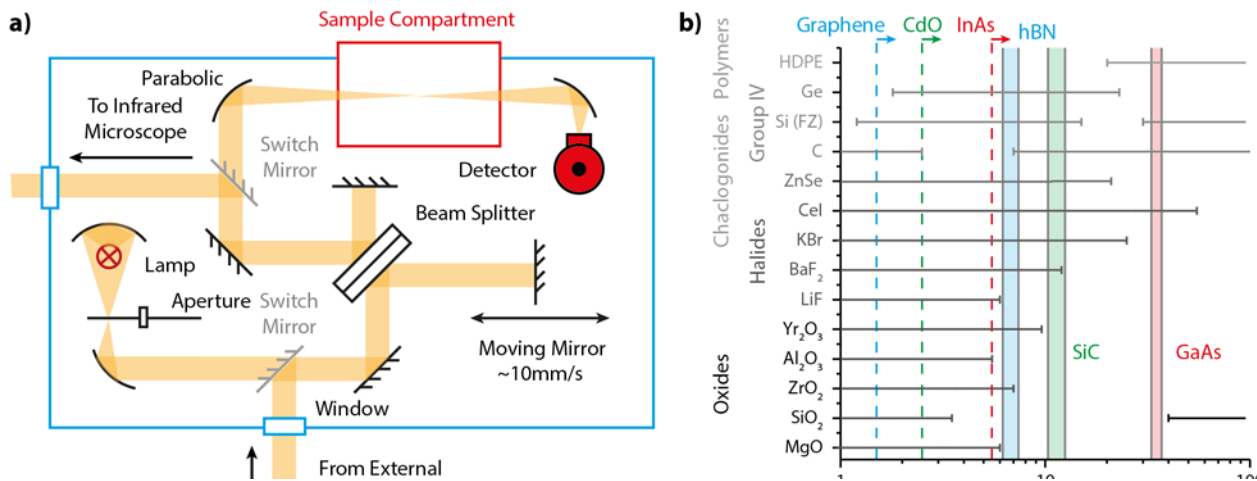

Figure 2: FTIR schematic and transmission properties of common infrared windows and substrates. (a) Schematic of an FTIR spectrometer configured for transmission and reflection, ATR and thermal emission measurements. (b) Common classes of IR transmission windows with the frequencies where polaritons can be supported for series of key polaritonic media. Filled bars indicate the Reststrahlen band of different materials and dashed lines indicate the maximum achievable plasma frequency for a conductor. Data for this plot is taken from the literature.[1,2-4]

It is also worth discussing the specific components used within an FTIR spectrometer, as these influence the overall system performance. Conventionally, an FTIR uses an incandescent bulb as a light source, using a filament designed to operate at a temperature providing the most light at a given IR frequency. For example, whilst a traditional tungsten-filament incandescent bulb is appropriate for NIR applications, a lower temperature silicon carbide glow bar is more conventionally used in the MIR. The next component is the interferometer and associated optics. Almost

all optics in the system are reflective, using gold- or aluminum-coated mirrors to enable broadband operation. However, the beam-splitter is required to be made of IR transparent materials, typically KBr (transparent from 25 µm into the visible, Fig. 2b). Short-wavelength measurements often use CaF_2 beamsplitters, while longer wavelength measurements (FIR to THz) usually employ Mylar beamsplitters, that will be discussed later in this tutorial. Typically, detection is achieved with one of two standard detector types – pyroelectric deuterated L-alanine-doped triglycene sulphate (DLaTGS) and cryogenically cooled photovoltaic or photoconductive mercury cadmium telluride (MCT) detectors. The former requires no external cooling, is extremely broadband (covering the full IR spectrum) and has a linear output, but is not very sensitive and has extremely slow response times (<1 kHz). MCT detectors can be extremely sensitive (approaching the photovoltaic limit[65]), and quite fast (tens of MHz, typically), but are slightly less broadband (conventionally ~20 to 1.3 µm, with a peak responsivity dependent on MCT alloy used), and generally exhibits nonlinearities in the output, limiting the dynamic range available for FTIR measurements. Finally, we also need to address the ambient atmosphere inside the FTIR. Atmospheric water and CO_2 have large absorption bands in the IR which can severely interfere with FTIR spectra. To prevent these gas-phase molecules from inducing artefacts into the desired collected spectra, it is important to purge the FTIR spectrometer with either CO_2-free nitrogen or air, or to hold the FTIR under a modest vacuum.

Reflection and Transmission

Reflection and transmission spectroscopy are the two most common and straightforward types of FTIR measurements. In both techniques a reference spectrum is collected, which consists of reflection from a metallic mirror (near-perfect reflection at IR wavelengths), or an open path for transmission and then the sample spectrum is collected and the two are divided. Transmission experiments are extremely easy to do within an FTIR – a sample is simply mounted in the sample compartment and the transmitted light intensity as a function of frequency can be directly collected. In addition, using various commercially available tools, a sample can be rotated with respect to the incident beam path, enabling angle-dependent transmission measurements. Due to the straight beam-path through the sample compartment, reflection spectra require an array of mirrors that allow the light to be incident on a sample at a fixed position, with the angle modified by controlling the mirror arrays in concert (see Fig. 3a for a schematic of such a tool). By performing correlated reflection and transmission experiments, it is possible to determine the extinction spectrum (e.g. total absorbed and scattered light), by using $E = 1 - T - R$, where E = A assuming negligible scattering (true for spectra of sub-diffraction resonators). However, in the IR both techniques have four major challenges. First – all common optical glasses are opaque in the IR. This means that substrates such as high resistivity silicon, germanium, or chalcogenide glasses, materials that are highly reflective or translucent in the visible, provide more appropriate IR windows. An extensive list of available IR window materials in reference to the operational range of several key polaritonic materials are provided in Fig. 2b as a guide. Second, the long wavelength of IR light makes these experiments extremely sensitive to etalon effects arising in high-index samples

9

and substrates that can significantly distort the spectral response. Third – conventional reflection and transmission measurements within the standard sample compartments can only be performed on samples relatively large in size, typically >1 cm^2, but with defined apertures can be made on regions of interest in the mm-range. Finally, an FTIR typically uses focusing mirrors that introduce some angular spread to the incident beam – this spread can artificially broaden the measured linewidth of resonances, including polaritonic modes due to their high sensitivity to incident angle. An example where such bench-based reflection or transmission measurements can be used for polaritonic experiments is the measurement of large-area arrays of polaritonic nanoparticles, gratings or dispersed nanoparticles. In all, reflection and transmission are routine experiments for measuring relatively large (>mm scale) samples of different polaritonic media.
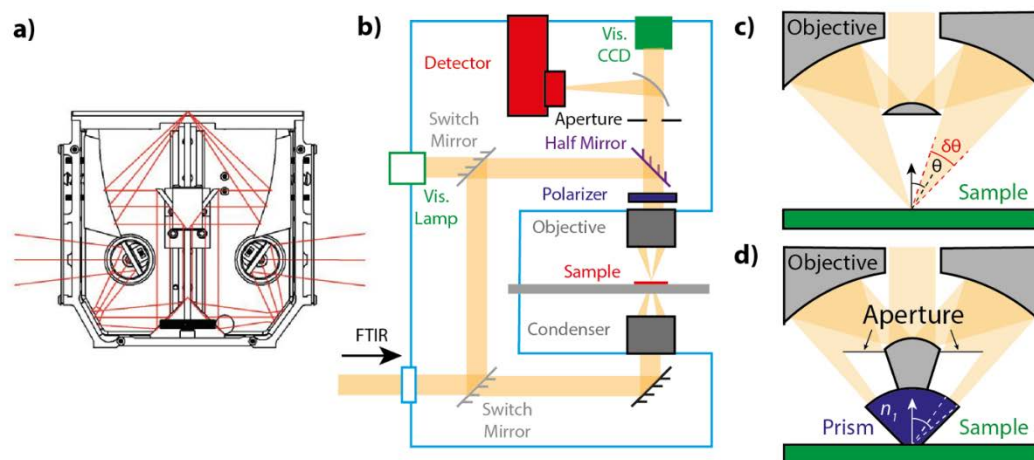

Figure 3: Optics for infrared reflection/transmission and ATR for variable-angle measurements in the bench and for microscope-based methods. a) Due to the linear beam path in the FTIR sample compartment, in order to perform reflection measurements, the light must be coupled into a multiple, coordinated mirror apparatus. A schematic for such a commercially available system (Pike Technologies) is provided here, highlighting how the four mirrors work in concert to focus the light to the sample position, albeit with a relatively broad incident angle spread. Note, that to change the incident angle, one simply needs to rotate these mirrors in concert so that the focal spot spatial position is maintained. Typically angles between ~30° and 80° are possible. (b) Microscope measurements effectively redirect the incident broadband beam from the bench sample compartment, making the microscope the defacto sample compartment. The optical path of a typical IR microscope, configured for viewing of the sample with a visible camera before IR reflection measurements is provided. c) For performing FTIR measurements in the microscope over a broad spectral range, Cassegrain-type objectives are required. A schematic of a typical Cassegrain objective, which has a weighted mean incident angle of approximately ~25 degrees, and a total angular spread of ~10°. d) Such objectives can be modified to accommodate a prism for the purpose of performing small area ATR measurements. A schematic of such an "ATR Objective" is provided. In d) an aperture is used to reduce the incident angular spread, which can also be applied in the context of c).[8,9]

Attenuated total Reflectance (ATR)

In many cases, pure reflection and/or transmission spectroscopy are not sufficient to collect the IR response of a material or film of interest. For instance, in thin films, such as polymers or thin dielectrics, the long-wavelengths associated with the IR significantly suppress the IR absorption cross-section. Within polaritonic media, the large momentum mismatch between free-space light and the surface polaritons (see Fig. 1a) also causes additional challenges. Attenuated total reflection (ATR) provides an avenue to overcome these challenges. In ATR experiments, light is directed to a sample surface through a prism of a high refractive index (Fig. 1b and c). Due to total internal reflection, when the incident light reaches the bottom prism surface, an evanescent wave is launched that propagates in the dielectric medium on the opposite side of that interface. For instance, in the Otto configuration experiment illustrated in Fig. 1c, this evanescent field propagates in the air-gap between the prism and the polaritonic material. In IR polaritonics, this evanescent field provides the additional momentum to overcome the previously stated mismatch, thereby enabling direct measurements of polaritonic absorption via prism coupling (Fig. 1 a-c). The ready availability of IR transparent, high-index materials (including ZnSe, Si and Ge, see Fig. 2b) makes this approach extremely appealing for measuring IR polaritons. It should be noted that as the polaritons excited in ATR experiments have in-plane momentum and out-of-plane evanescent fields, they are only launched by *p*-polarized light, so comparisons between the angle dependence of *p*- and *s*-polarized ATR spectra allow for easy identification of polaritonic modes from other absorptive modes within the material (e.g. IR active phonons or vibrational bands).

The direct measurement of polaritons via ATR methods can be achieved in one of two configurations. Through-film coupling termed the Kretschmann-Raether or Kretschmann configuration, relies on bonding or pressing a polaritonic film onto the surface of the prism (Fig. 1b). In this approach, the evanescent field induced at the prism-polaritonic-medium interface can launch a polariton, provided the skin-depth of the evanescent field extends to the opposite side of the polaritonic material. This can provide a very simple approach to measuring the polaritonic dispersion, specifically aided by changing the incident angle and/or the index of refraction of the prism, both of which directly change the momentum of the incident light. However, while bonding a polaritonic film onto a prism is effective, films can be difficult to remove making the experiment difficult to repeat, and in many cases, destructive. In addition, pressing a sample onto a prism requires a dielectric substrate on which the polaritonic medium is grown or deposited. However, for polariton excitation to be possible, the substrate must have a lower index than the prism (otherwise the optical mode is 'pulled' into the substrate).[8] Furthermore, excellent optical contact needs to be achieved between the substrate and the polaritonic film, which can be problematic with stiff materials. Thus, a commonly used alternative involves coupling to the polaritonic mode through an air gap (Otto configuration, Fig. 1c), which is a much more versatile approach, as a clean interface between sample and prism is no longer required, and the substrate has a less significant effect. However, the position between prism and sample

11

needs to be precisely controlled at a length-scale below the compressed polariton wavelength. This has been achieved using piezo stages and interferometers to accurately calibrate the prism-sample distance.[53,66] In the case of Otto experiments, the momentum can again may be modified through changing the incident angle and/or prism material, but additionally by changing the size of the air gap, the evanescent extent of the mode can be probed. An optimal overlap between the evanescent field from the reflection at the prism surface and that of the polaritonic medium occurs, with this condition deemed the 'critical coupling' point.[12]

Thermal Emission and Emissivity Measurements

Beyond reflection and transmission, the strong absorptive nature of polaritonic resonances provides an alternative method for probing their response. This can be realized through measuring thermal emission from a sample. For room and elevated temperatures, from 300-1400K, the peak black-body emission from a surface inherently occurs within the mid-IR. While a perfect blackbody emits in accordance with Planck's Law of Blackbody radiation, with a peak emission occurring at the Wien wavelength, for any real surface, this thermal emission is modified by the spectral dependence of the emissivity of the surface. Kirchhoff's law of thermal emission tells us that the absorptivity is equivalent to the emissivity at the same temperature $\epsilon(\lambda) = \alpha(\lambda) = 1 - R(\lambda) - T(\lambda)$, where $R(\lambda)$ is the surface reflectivity and scattering is assumed to be negligible. Within polaritonic nanostructures, specific resonant modes will result in narrowband absorptive antenna resonances, which as stated above provide narrowband resonances in the emissivity spectrum. Therefore, when heated to elevated temperatures, these resonances will produce strong narrow-band thermal emission, with the irradiated power dictated by the emissivity and the temperature-dependent thermal energy available.[22] In addition, by controlling the periodicity of the polaritonic structures, the spatial coherence (directivity) of the thermal emission can be controlled,[6] while through implementing anisotropic nanostructures the emitted light can be polarized into the far-field.[21,22] Thus, one particularly intriguing opportunity for IR polaritonic materials is the design and demonstration of spectrally or spatially selective thermal emitters. Moreover, measuring thermal emission from polaritonic nanostructures can also provide direct observation of the resonances and therefore provides an extremely useful platform for characterizing polaritonic nanostructures[22] and in some cases thin films.[54,57,67-70]

It is relatively easy to measure thermal emission spectra from a sample in a FTIR spectrometer by using the sample as a light source, provided the interferometer is configured appropriately. However, the collected spectrum is not a calibrated measurement of the sample emission or emissivity.[71] The spectrum that is measured $S(\lambda, T_i)$ contains the sample emission at a given temperature T_i, designated as $s(\lambda, T_i)$, and a blackbody thermal background from the FTIR optics $r(\lambda)$. Furthermore, this sample emission and thermal background are multiplied by the spectral responsivity of the FTIR, $R(\lambda)$. The measured spectrum can then be expressed as $S(\lambda, T_i) = R(\lambda)(s(\lambda) + r(\lambda, T_i))$. The simplest way of correctly calibrating an FTIR therefore is to compare the measured spectrum of a blackbody

12

at two different temperatures $B(f, T_i)$, with the spectra for an ideal black body $b(f, T_i)$ for calibration. Using these two measurements, we can write;[72]

$$R(\lambda) = \frac{B(\lambda, T_2) - B(\lambda, T_1)}{b(\lambda, T_2) - b(\lambda, T_1)} \qquad (4)$$

$$r(\lambda) = \frac{B(\lambda, T_1)}{R(\lambda)} - b(\lambda, T_1) \qquad (5)$$

This calibration procedure can be used to estimate the emissivity of a sample relative to the reference. By taking the ratio of the calibrated spectra to that of an ideal black body, one can extract the emissivity spectrum of the sample at the measured temperature.[73] Note that finding a material which serves as an accurate black body reference is extremely challenging, as materials typically exhibit temperature-variable emissivity. At temperatures below 600 K, a layer of soot deposited using a candle acts as a reasonable approximation, however self-absorption of the thermal emission can occur within thick films and thus care must be taken in the optimizing the preparation conditions.[74] More recently, arrays of carbon nanotubes have also been deployed as more robust black body references.[71] Back-reflections into the interferometer from the detector can also play a significant role in calibrating these measurements at low temperatures. For weak thermal emitters (where the emitter temperature is less than the temperature of the detector or the FTIR optics, the situation becomes even more complicated, as the relative phase difference of the emission from the source, beam-splitter, and detector must be taken into account.[73] Although a discussion of these effects is beyond the scope of this tutorial, early FTIR work offers insight as to how best to approach these challenges.[73,74]

FTIR Microscope Measurements

The techniques mentioned above all use bench-based measurements within the sample compartment of a FTIR spectrometer (Fig. 2a), thereby implying low magnification and the requirement for relatively large samples. However, it is also possible to do micron-scale sampling using a specially designed FTIR microscope. This is particularly important for polaritonic antennas fabricated using top-down approaches, as arrays are typically small, in the range of tens of µm on a side. In such approaches, the IR beam is passed through the interferometer and then out to the microscope, which contains specialized IR objectives, and then typically into a microscope-mounted liquid-nitrogen cooled MCT detector. In this way, the microscope acts as the 'sample compartment', offering higher magnification and therefore the ability to measure small regions of interest (Fig. 3b). However, the objectives used for IR microscopy require special discussion. While refractive objectives using IR transparent materials such as ZnSe or Ge are available, these components have restricted spectral bandwidths due to the anti-reflection coatings and inherent spectral dispersion of the materials. More conventionally, reflective objectives, with a Cassegrain design consisting of two opposing mirrors, are employed (Fig. 3c). These objectives are capable of measuring samples in both reflection and transmission geometries. In the case of the latter, a condenser must be paired with the objective that provides the ability to compensate for the index of refraction of the substrate so that the focal

13

point can be positioned at the sample of interest. Specialized objectives are also available that can perform ATR measurements using a prism with a front face only 100 µm across (Fig. 3d), while others are available for grazing-incidence measurements where the light can be directed to a micron-scale region of interest at angles on the order of 70° with respect to the surface normal. These are especially well-suited for thin film absorption measurements or performing polaritonic dispersion measurements on small-area flakes or regions of interest.[8] In general, the FTIR objectives offer moderate magnification factors (15x and 36x are standard), and a Cassegrain objective does not excite or collect at normal incidence light (see Fig. 3c). This has important implications for the excitation (and measurement) of propagating polaritons in experimental systems, as the wide range of angles for the incident light will generally blur any spectral features associated with the momentum-matching requirements for coupling to propagating modes. For localized polaritonic antenna resonances this ensures that both in- and out-of-plane excitation will occur simultaneously for all standard collection conditions.

Infrared microscope objectives do not focus the IR light to a diffraction-limited spot, but instead focus into a spot size on the order of hundreds of µm. To measure samples smaller than this beam-spot, apertures are used to define the region of interest. While in principle this area can be as small as 5 µm, in practice this significantly reduces the optical throughput of the system, and the diffraction limit begins to prevent the propagation of long-wavelength IR light, and correspondingly the spatial resolution of any measurement. Thus, while this technique can be used to effectively map out IR spectra across different spatial positions on a non-uniform sample, an alternative route is to use a focal plane array (FPA) attached to the IR microscope in place of the aforementioned detector. An FPA is a detector array, allowing the collection of a hyperspectral image across the full microscope field of view. As a result, this is an extremely effective way of collecting IR spectra over a large area simultaneously, though IR FPAs are orders of magnitude more expensive than their short wavelength counterparts and are not commercially available at wavelengths much past the long-wave IR (~800 cm^{-1} as low frequency cutoff for FTIR microscope mounted systems).

Modulation spectroscopy

Beyond the collection of optical spectra, FTIR also offers opportunities for performing time-dependent and lock-in amplifier integrated measurements. In conventional FTIR spectroscopy the mirror is continuously scanned, and the detector signal is continuously monitored. However, in another mode of FTIR called 'step-scan', the mirror is stopped at a series of different positions, and a time-dependent response can be collected, assuming the optical phenomena is repeated for every mirror position. For each time point, the interferogram can be collected and a FT can be performed to extract a spectrum. By using a fast analogue-to-digital converter, spectra can be collected with as fast as 2.5 ns temporal resolution. This approach can be implemented for performing pump-probe measurements (though typically not with the time-resolution required to observe the characteristic timescales of polaritons or the

14

associated fundamental charge oscillations). The same step-scan approach can be used to collect a lock-in amplifier integrated spectrum for extracting the differential IR response of materials under optical or other external stimulus. Instead of measuring a time-dependent signal at each interferogram point, the lock-in amplifier integrated signal can be collected at each interferogram point. This technique allows the measurement of modulated spectroscopies, such as photo- or electro-reflectance, or modulated emission from IR materials.

Laser-Based Spectroscopic Methods for Probing Polaritons

FTIR-based characterization of IR polaritonic materials and structures offers valuable broadband spectral information about the polaritonic modes they support. However, such measurements typically employ incoherent light sources, which are difficult to focus and collimate. Collimated beams from internal FTIR sources can be used to spectrally interrogate large-area, periodic structures, but are of little utility for investigation of individual polaritonic structures or for visualization of polariton propagation across the surface of a sample. This is because polariton propagation lengths are often significantly smaller than the spatial extent of the probe beam. More localized investigations of polaritonic surfaces are achievable with incoherent FTIR sources, typically using all-reflective large numerical aperture (NA) objective lenses in an IR microscope, as discussed above. However, such an approach is poorly suited for characterization of propagating polaritonic modes, as coupling to free-space light into these modes is strongly angle-dependent, and the large NA of the IR objective lens ensures a broad range of incident angles for the probe beam, washing out any angle-dependent spectral features.

Most of the challenges outlined above are alleviated through the use of a coherent probe beam, which allows for significant reduction in the incident spot-size and angular resolution, although this is achieved at the expense of spectral bandwidth. Historically, the coherent sources available in the IR were limited to a number of gas lasers, specifically the HeNe (3.39 μm) and CO_2 (9.5-11 μm) lasers,[75] with the latter utilized to demonstrate critical coupling to SPhPs at $\lambda \sim 10.8 \mu m$.[76] Alternatively, free-electron lasers and IR synchrotron radiation offer broadly tunable, coherent sources for excitation and characterization of IR polaritonic modes, though the cost and size are unsuitable for future polariton-based optical systems and optoelectronic devices.[77,78] The advent of the quantum cascade laser (QCL)[79] and its counterpart the interband cascade laser (ICL),[80] have provided compact, wavelength tunable, high power, commercially available coherent sources across a wide range of IR frequencies. The narrow linewidth and collimated nature of the IR light from a QCL allows for angle-resolved coupling to propagating IR surface modes on metallic films. Such coupling has been demonstrated in the Kretschmann geometry (using a Ti/Au-coated CaF_2 prism) for measuring CO absorption,[81] or alternatively for probing the coupling to, and propagation of, IR surface modes on extraordinary optical transmission (EOT) gratings[82] or corrugated beam-steering or beam-shaping structures.[83] Though the emission from QCLs and ICLS is generally narrow band,

spectroscopic characterization is possible using broadband gain media, fabricated into arrays of addressable narrowband emitters, or alternatively, using external cavity tuning.[84]

In parallel with the development of cascade lasers, significant improvements in fiber-based IR light sources over the past decades have resulted in viable alternatives for IR applications. These light sources often leverage fluoride-, telluride- or chalcogenide-based fibers, either doped with rare-earth ions to form an optically-pumped IR gain medium,[85] or alternatively, leveraging non-linear optical effects in highly nonlinear step-index or micro-structured IR-fibers. Such sources can achieve ultra-fast supercontinuum pulses using either ultra-fast mid-IR pumps,[86] or alternatively, concatenated fibers designed to generate a supercontinuum in successive long-wavelength bands.[87] IR fiber lasers not only offer reasonably compact sources for probing the optical properties of IR materials and structures, but also the opportunity to probe IR polaritons on time scales commensurate with ultrafast carrier and lattice excitation dynamics. Such sources have led to a wealth of time-resolved experiments, most frequently combined with the spatially resolved experimental techniques discussed in the next section.

Not only have the new generation of mid-IR sources allowed for more effective probing of IR polaritonic modes, but recent work has demonstrated the potential utility of polaritons for the design and demonstration of new types of sources operating in this spectral range. Patterned metallic structures, fabricated directly onto the facet of a QCL, have been used to demonstrate highly directional, polarization-controlled collimated beams.[88] In this work, light at the laser facet is coupled via a subwavelength slit to propagating surface modes (polaritons) on the metal-coated laser facet. Structures patterned onto the laser facet then scatter the surface modes with a carefully designed phase relationship, resulting in directional light emission, with control over the emitted beam shape and polarization state.[88,89] Such devices offer unique control of the IR light by direct integration of polariton-supporting structures onto the laser output. Alternatively, IR polaritonic structures have been directly integrated into IR gain materials, a prime example being the so-called plasmonic waveguides used as the mode-confinement mechanism for some early QCLs.[90] Though such waveguiding structures were largely discarded due to the lower loss afforded by all-dielectric waveguides, recent work has explored the potential of SPhP waveguides for far-IR QCL devices. In these emitters, thin slabs of polar materials are used to support SPhP modes for QCL designs with low-energy intersubband transitions, offering a route towards phonon-polariton enabled sources for far-IR wavelengths.[91] Such emitters mark the first compact sources with the potential for characterization applications at far-IR frequencies (a wavelength range currently devoid of coherent sources), though they are as of yet limited to narrow wavelength bands around the LO phonon energies of III-V materials that are lattice-matched to QCL architectures.

The coherent sources discussed above offer narrowband, high-power, and in some cases, ultra-fast IR sources for characterization of IR polaritonic materials and structures. The coherent nature of the light emission offers the opportunity for high power, collimated probes, as well as high-speed modulation for lock-in measurements. In general, coherent sources offer reduced spot sizes for spatially-resolved probing of IR materials and devices, though

these spot-sizes will always be diffraction-limited in any set-up using standard optical components. In the subsequent section we discuss the significant advances in sub-diffraction-limit characterization of IR materials and devices that can be achieved by leveraging coherent sources and a new generation of IR imaging technology.

Nano-probe-based Methods for Spatial and Spectral Characterization of Infrared Polaritons

Both FTIR and laser-based spectroscopies are inherently constrained by the diffraction limit of IR light – which is almost always above a micron across the IR portion of the electromagnetic spectrum. Infrared characterization took a significant leap forward in the late 1990's with the advent of scattering-type scanning near-field optical microscopy (s-SNOM).[7,92] This development allowed for coherent IR light sources to be coupled into an atomic-force microscope (AFM), thereby combining the ability to experimentally probe light-matter interactions well below the diffraction limit, while also collecting topographical information about a sample (schematic provided in Fig. 4). In regards to IR nanophotonics these capabilities of s-SNOM were transformational. For the first time there existed an experimental probe that could quantify the frequency-dependent optical behavior of a material or structure with spatial resolution on the order of the length-scale of the polaritonic effects.

The methodology for the s-SNOM technique is based upon the scattering of incident light by a metallized AFM tip,
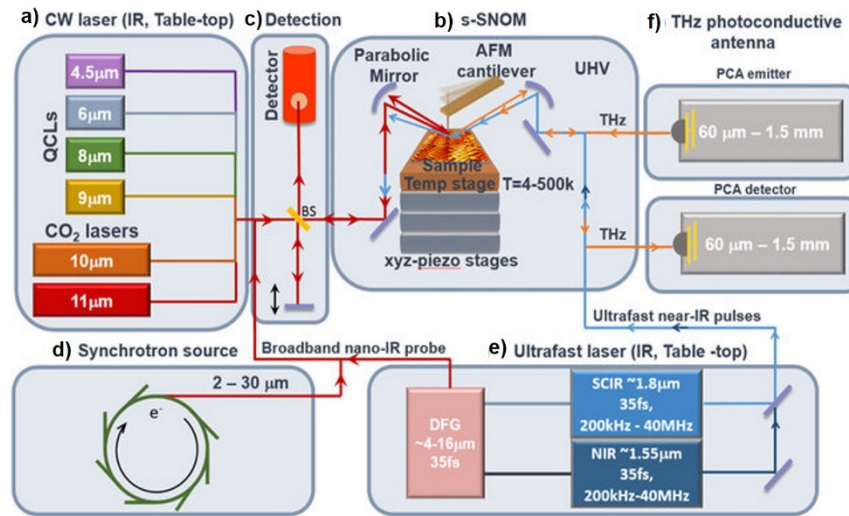

Figure 4: Schematics of scattering-type scanning near-field optical microscope (s-SNOM). (a) CW laser sources (b) ultra-broadband synchrotron light source (c) table top ultrafast broadband IR laser source (d) table top THz broadband sources utilizing photoconductive antennas (PCA) (e) AFM-based near-field platform with optics and sample stages. (f) Interferometric detection. Light is directed to the AFM tip via parabolic mirrors. The scattered light is then directed from the sample to an additional parabolic mirror, which is collected using an appropriate detector. Figure modified from Ref. 7.

providing a strong scattering element for incident, continuous-wave IR light (Fig. 4a). The implementation of an AFM is critical for multiple reasons. First, the scattering induces strongly *p*-polarized (along z-axis) evanescent fields with high wavevectors that are induced within nanometer-scale proximity of a sample surface. In the case of polaritons, this is essential as the high-k provides the means to overcome the momentum mismatch between free-space light and the polaritonic modes.[92] The implementation of tapping-mode AFM for these measurements also enables the optical signal to be extracted at multiple harmonics of the

17

AFM-tip oscillation frequency using a lock-in amplifier to more efficiently filter the incident fields from those corresponding to the local near-field response (Fig. 4b). In practice, each higher harmonic improves this filtering, but also comes with weaker signal strength. Typically for polaritonic measurements the 2nd to 4th harmonics are plotted. Finally, the AFM configuration and heterodyne detection scheme (Fig. 4c) allows for simultaneous mapping of the optical amplitude and phase, along with the topographic information of the sample. This spatial mapping therefore enables imaging of polariton propagation,[2,10,39,41,50] identifying material-specific optical modifications,[28,93] demonstration of hyper- and superlensing concepts and designs[94] and the electromagnetic field distributions of localized surface polariton antennas.[22,95]
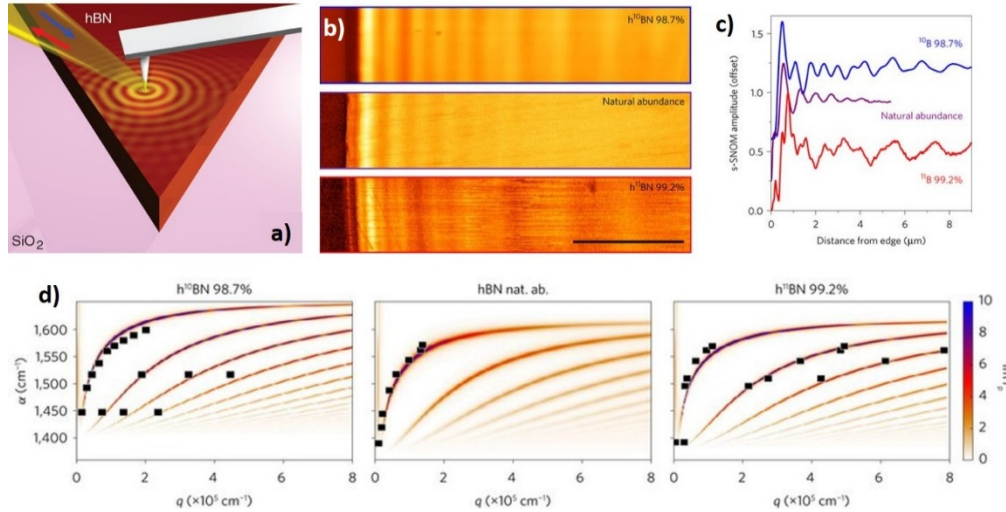

Figure 5: a) Schematic of an IR light being scattered off of an AFM tip, launching radial polaritonic waves. When the polariton waves reach the edge of a flake, they are reflected, interfering with the launched wave forming the interference patterns with a periodicity of $\lambda_{polariton}/2$, this is shown here for hexagonal boron nitride that is isotopically enriched with 98.7% ^{10}B (top), 99.2 ^{11}B (bottom) and in its naturally abundant form (center). c) By extracting linescans and performing a fast Fourier transform, the spatial frequency at that incident frequency can be extracted. d) By plotting the spatial frequency at multiple incident frequencies, the polaritonic dispersions can be extracted. Note that here, due to the hyperbolic nature of hBN that the isotopically enriched flakes (left and right) exhibit higher order modes shown as high q (shorter $\lambda_{polariton}$) polaritons at the same incident frequency. a) From Ref. 10 b)-d) from Ref. 2.

Perhaps one of the most powerful features of s-SNOM methods for characterizing polaritons is in the ability to directly image the wavelength of a propagating mode.[2,10,39,41] Initially realized with metallic elements fabricated on the top of SiC to focus SPhPs launched by the s-SNOM tip,[96] it has since evolved into a method for extracting the polariton dispersion relationship.[2,10,39,41,97] Demonstrated by the Koppens and Hillenbrand[39] groups simultaneously with the Basov group[41] for SPPs in graphene, this method requires the implementation of a sharp edge that can serve to reflect the tip-launched wave, and in many cases directly launch the polaritonic waves, resulting in an interference pattern. This has been demonstrated quite elegantly within nanoscale thickness slabs of hexagonal boron nitride (hBN).[10] This is shown in Fig. 5a-d for hBN. Initially, the scattering of the incident light from the tip couples to higher momentum polaritons, launching a radially propagating mode (Fig. 5a). This mode continues to propagate radially, until reaching a sharp boundary (e.g. flake edges in Fig.

18

5b) the wave is then reflected, establishing an interference pattern between the forward- and backward-scattered waves. Additionally, direct launching of the polariton can also be induced due to scattering off of the flake edge or boundary, resulting in two different interference patterns with periodicities of $\lambda_{sp}/2$ and λ_{sp} for tip- and edge-launched polaritons, respectively.[98] By extracting a series of linescans normal to the flake edge (Fig. 5c) and performing a Fourier transform, k_{sp} (λ_{sp}) of the polaritonic mode can be extracted. By performing this as a function of incident frequency, the polariton dispersion can be experimentally determined (Fig. 5d). This has several specific implications with regards to this tutorial. This implies that measuring the polariton dispersion provides an avenue to determine many material-specific properties of interest for IR nanophotonics, for instance the optical conductivity (dielectric function for bulk semiconductors), Fermi energy and scattering rate for free-carriers, or phonon scattering and energies for polar materials with spatial precision that can even surpass the radius of curvature of the s-SNOM tip. Thus, this method can also be utilized for probing subsurface features[99] or for characterization of defects in semiconducting materials and devices.[100]

Within nanostructured polaritonic antennas, s-SNOM can provide a means to directly map the localized electromagnetic field profiles. Such spatial maps can be directly compared to calculated field profiles using commercial solvers to validate theory.[22,95] However, the use of a metallized AFM tip can cause modifications to the fields due to the large dipolar field associated with this additional antenna and its non-trivial interaction with the polaritonic dipole(s). Thus, to avoid such effects, one may implement a dielectric (typically Si) tip that can be used to extract the topographic and optical fields, without serving as a significant source of polariton launching. This was demonstrated for mapping the localized modes of SiC SPhP bowtie antennas.[22] However, to be able to map the resonant modes, one must first know the spectral position of the antenna resonances, typically extracted by far-field FTIR measurements of periodic arrays of the antennas of interest. However, there does exist a spectral shift between the far- and near-field resonant conditions due to the presence of the s-SNOM tip,[95] and thus the far-field measurements only provide a rough estimate of the spectral position. Therefore, ideally one should measure the near-field spectra in the presence of this tip, which can be achieved through the implementation of a broad-band light source for nano-FTIR,[101] providing direct measurements of the local spectral response.

In contrast to s-SNOM, nano-FTIR utilizes a broad-band coherent light source [e.g. a synchroton or difference-frequency-generation-based broad band laser (Fig. 5d)] with an interferometer similar to an FTIR system, but coupled through the s-SNOM apparatus (Fig. 5c). In the case of slabs of polaritonic media, nano-FTIR can provide a means for directly extracting the polaritonic dispersion at low-k within a single measurement, as in Ref. 10,47. In the context of localized antenna resonances, nano-FTIR can provide direct measurement of the resonance spectra.[95] When compared with the corresponding far-field reflection and/or transmission spectra, nano-FTIR offers the ability to quantify the degree of linewidth broadening that results from inhomogeneities within the nanostructure geometry among the periodic lattice in addition to measuring the IR spectra within the local dielectric environment

19

of the s-SNOM tip.[95] More recently, time-dependent methods have been developed enabling the imaging of the group and phase propagation of polaritons. For hBN, nano-FTIR was used to demonstrate the positive (negative) group (phase) velocity of the hyperbolic polaritons within the upper Reststrahlen band, along with direct measurement of the HPhP lifetimes[47,50] within both the lower and upper bands. Building on this, ultrafast pump-probe lasers have since been integrated (Fig. 5e),[102,103] allowing measurements of polaritonic near-fields under strongly non-equilibrium conditions such as in the presence of high free-carrier densities.

While s-SNOM has provided significant advancements in our understanding of IR nanophotonic materials and devices, it is still limited by the availability of coherent continuous-wave laser sources at frequencies below the long-wave IR (roughly 11 µm for s-SNOM, 15.4 µm for nano-FTIR). This limited spectral coverage extends out to the THz (Fig. 5f), where s-SNOM measurements are also possible.[104] The lack of coherent continuous-wave laser sources can be overcome by integrating the s-SNOM with a synchrotron (Fig. 5d) as demonstrated by the Raschke group,[105] however, this is not an accessible option for research groups that are not associated with such facilities. A complementary method that can integrate pulsed lasers and implements a mechanical read-out of local thermal expansion due to resonant excitation of a material or structure is the photothermal induced resonance (PTIR) technique,[106,107] which has the same operating principle as the photo-induced force microscopy (PIFM) method.[108] In these techniques, a pulsed laser illuminates a metallized AFM tip as in s-SNOM, however, the tip is typically operated in contact mode and the optical signal is read-out via nanoscale thermal expansion of the film or nanostructure being probed.[106,108] This mechanical read-out implies that these techniques measure the local absorption of light due to polaritonic resonances. As well as the ability to probe the local fields associated with strongly scattering optical modes that can be measured in s-SNOM, it is also sensitive to dark or weakly scattering modes,[106] as recently demonstrated by the Caldwell and Centrone groups. Furthermore, the ability to implement pulsed-laser sources within this methodology also extends the spectral range for these measurements into lower frequency regimes, however, this is still currently limited from extending into the far-IR due to the lack of appropriate laser sources. However, the PTIR/PIFM methods are still in the nascent stage in terms of their use for polaritonic characterization and thus offer significant promise as complementary characterization tools for polaritonic materials and devices in the years to come.

Complexities for Probing Polaritons within the Far-IR (FIR)

As it is for the MIR, the FTIR is also the spectroscopic workhorse for FIR measurements. However, FTIR spectroscopy in the longest wavelength portion of the IR, though similar in general experimental set-up to its MIR counterpart, comes with a number of additional challenges. For broad-band spectroscopic applications, the bench top available light source is often the same SiC globar. The utility of this source is largely limited by the high operational temperature of the bar, which by Wien's law, puts the bulk of the IR thermal radiation at much shorter wavelengths, which produces limited additional FIR power with further increases in globar temperature. Moreover,

20

the sub-unity emissivity of SiC at such long wavelengths also contributes to the weak spectral power density as one moves further from the blackbody emission peak. Alternatively, mercury vapor lamps can be used as FIR sources, offering marginal improvement in spectral power density within this range, resulting from near-unity emissivity across the majority of the 20-60 µm spectral range. However, mercury vapor lamps typically require water-cooling, and thus have a sizeable footprint. High power, coherent emission has been realized with free electron lasers (FEL),[53,66,77,109] synchrotrons,[105] and molecular lasers, but all of the above are costly and poorly suited for compact, bench-top applications.

The dearth of FIR sources are far from the only obstacle facing spectroscopic analysis at such long wavelengths. FIR beam splitters are similarly suboptimal compared to their MIR counterparts. The beam splitter of choice for the FIR is typically made of a single thin Mylar film, or alternatively, multiple thin films of Mylar. Unfortunately, the response function of thin film Mylar is far from uniform or broadband, due to absorption in the Mylar (~100 cm^{-1} across the FIR)[110] and variations in the film thickness across the beam splitter. Stacking multiple thin films increases the bandwidth of the beam splitter at the expense of increasing absorption and the introduction of additional absorption features. Furthermore, Mylar is microphonic, so laboratory vibrations can reduce the sensitivity of the interferometer. Another potential FIR beamsplitter material is CsI, which has a well-behaved response function over the FIR. However, the highly hygroscopic nature of CsI makes it unsuitable for applications requiring extended exposure to atmosphere, and only operates down to 150 cm^{-1}. It is also worth noting that Mylar and CsI windows are used as viewports for evacuated FTIRs and for FIR detectors. Often the CsI is coated in a thin layer of polyethylene to prevent environmental damage.

The two primary detector classes used in the FIR are the pyroelectrics (LiTaO$_3$, DTGS, and the improved DLaTGS) and bolometers (Si and superconducting). As previously mentioned, pyroelectric detectors can detect light across the entire FIR spectrum with a flat and linear response across a broad range of FIR frequencies, both important for FIR spectroscopic applications. However, they have significantly lower sensitivity (specific detectivity, or D*$=\sqrt{Af}$ / NEP of ~10^8 Jones) compared to bolometers (D*~10^{12} Jones) and have severely limited response times, usually on the order of 1 to 10 Hz, making them susceptible to 1/f noise. Furthermore, pyroelectrics are often piezoelectric, so vibrations from the lab can further reduce the sensitivity of these devices. Bolometers offer a significant increase in sensitivity, ~3-4 orders of magnitude, and modulation speeds into the kHz, but require either liquid helium, or expensive cryo-free systems to cool the detector element to liquid helium temperatures (4.2 K) using closed-cycle compressors.

As a rule, the speed of detectors in the FIR is severely limited compared to those operating in the MIR. This makes time-resolved measurements essentially impossible. Even step-scan measurements, which are based on the modulation of the signal on the FIR detector, can be incredibly time-consuming, as step-delay and lock-in amplifier signal integration times will have to be comparable (but at least ~3x longer) than the detector response times. One

21

approach to overcome the slow detector response is to use detector window materials that are only transparent in the spectral range of interest. Alternatively, additional filters can be placed in the optical path to pass only light in this small spectral range of interest. This filtering allows one to take larger steps in mirror position in step-scan mode and therefore attain shorter total scan times. Zero transmission outside the filter passband is required as the larger mirror steps can be conceptualized as folding the entirety of the optical spectrum into the wavelength range of interest. Any signal outside of the filter passband is therefore folded into the wavelength range of interest, resulting in artefacts which cannot be easily separated from the 'real' spectra.

The emission from the experimental optical components becomes even more important in the FIR, especially when measuring emission from samples colder than your detector and beam splitter. Given a weak sample emission, if one were to subtract the self-emission of the FTIR in spectral space, they would likely find spectral regions with negative emission. One method of overcoming emission from the interferometer is to cool the entire system to cryogenic temperatures. Obviously, evacuating and cooling all the optical components in an interferometer introduces a plethora of additional problems. An easier method to overcome self-emission of the FTIR is to leverage the phase difference between the detector and the beam-splitter emission relative to the sample. All one has to do is subtract the self-emission of the FTIR in interferogram space rather than spectral space and then compute the discrete FT, with a high phase resolution, of the subtracted interferogram.[73]

IV. EXAMPLES AND APPLICATIONS

1. Semiconductor Nano-resonators for Surface Sensing

As discussed in section II, nanoresonators offer one of the simplest routes to coupling far-field radiation into a surface polariton mode, manifesting as resonant absorption, transmission or reflection in its spectral response. As localized resonators concentrate the electromagnetic field close to the surface of the sample, this allows them to be used for sensitive surface sensors. In this case, the change in the local dielectric environment caused by the presence of an absorbing molecule or film on the surface of the resonator causes a frequency and amplitude shift in resonant modes. This shift is detected using either FTIR or laser-based spectroscopy techniques. Localized polariton nano-resonators in the IR can be realized using both SPP and SPhP modes in semiconductors – in this case we examine structures formed of doped InAs[30,111] and SiC[3,22,112,113]. InAs has a low electron effective mass and can be doped over a large range of carrier concentrations, maximizing spectral tunability for associated SPP modes, while it may also be spectrally tuned or modulated using continuous-wave visible excitation due to free carrier injection as was recently demonstrated for InP.[31] SiC can be grown on a wafer scale with long phonon lifetimes and hence low material losses, featuring a Reststrahlen band in the long-wave IR.[3,28,114] This makes both of these materials ideal for localized surface polariton resonators.
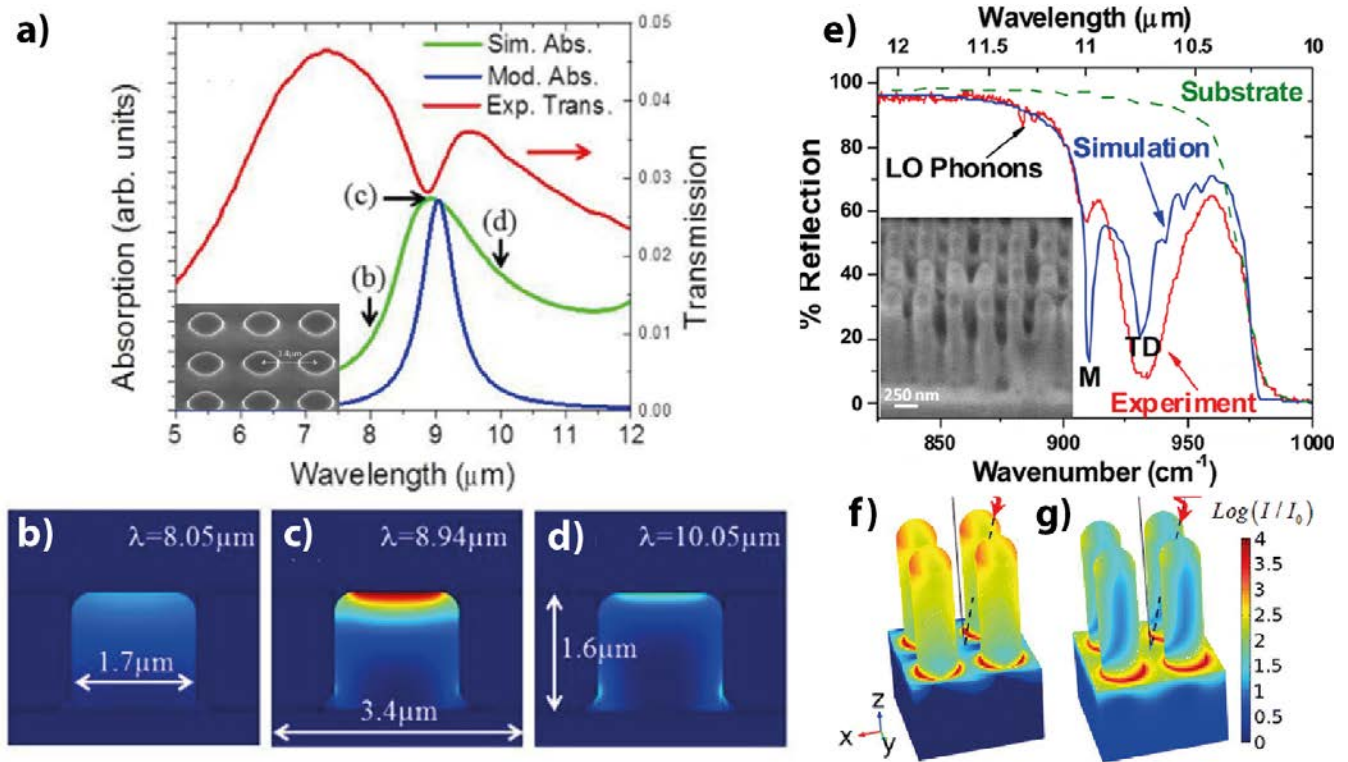
22

Figure 6: a) Absorption and transmission spectra collected using an FTIR microscope from nanostructures fabricated from highly doped InAs (Inset shows SEM image of sample at 45 degrees incidence). The simulated electromagnetic loss profiles field profiles in b-d were calculated for the frequencies denoted in a). e) Experimental and simulated long-wave IR spectra from periodic arrays of SiC nanopillars (inset: SEM image of representative array), using an FTIR microscope. Two distinct resonances with significantly different electromagnetic field distributions were observed, designated as the f) transverse dipole (TD) and g) monopole (M) resonances.

In Ref. 29 films of InAs with various carrier concentrations were grown by MBE and subsequently patterned into nanoresonators (inset Fig. 6a). The films were characterized by a combination of electrical transport measurements and FTIR microscopy (Fig. 6a), which allowed accurate determination of the opto-electronic properties for each sample. It was found that the plasma frequency could be tuned significantly by doping, from approximately 5-15 µm. This is critical for achieving resonances over a broad range of frequencies, however, it should be noted that the mobility drops significantly as the doping density is increased. Resonators formed from these films supported a localized SPP mode, which can be verified through careful comparison with numerical simulations (Fig. 6b-d). Subsequent work[111] demonstrated that by careful design of both the plasma frequency and the resonator size, the polariton resonances can be tuned. Furthermore, the localized SPPs modes were used to detect the presence of a PMMA membrane, demonstrating the ability to create localized infrared surface sensors.[111] It is worth noting that similar results can be achieved by utilizing a grating geometry[38], where almost perfect absorption can be achieved,

though the periodic nature of such sensors precludes the development of subwavelength localization of the probe field in all three dimensions.

An alternative approach to obtain narrow-band polaritonic resonances is through the fabrication of such structures using polar crystals capable of supporting SPhPs. Such resonators were fabricated into a SiC substrate using electron beam lithography and reactive ion etching and characterized using FTIR microscopy.[3] Extremely sharp resonances were observed, with quality factors in excess of 100 and confinement factors of up to 200x smaller than the free space wavelength reported, which occurs due to the inherently low losses of this material (See Fig. 6e). Subsequent work on similar nanostructures in SiC were shown to have record quality factors in excess of 300,[112] while work within hBN nanostructures exhibited values as high as 286.[62] Each of the different resonances is associated with a different electromagnetic mode - which can be characterized by comparison against numerical simulations (Fig. 6f and g). These resonances can be individually tuned to some degree by changing size or aspect ratio of the particles,[22,112,113,115] which can also be used to produce a dependence of the excited resonance on light polarization.[21,22,113,115] While the narrow spectral window in which these resonances can be measured notably limits some applications, these extremely sharp resonances have continued to motivate the study of SPhP resonators. For example, SPhP in SiC have been exploited for surface sensing, with detection possible down to a few atomic layers,[15] while hBN resonantors have been demonstrated for femtomolar sensitivity using the surface enhanced IR absorption (SEIRA) effect.[116]

2. Investigating Narrow-band and Spatially Coherent Thermal Light Sources

The strong absorption of polaritonic modes, and the ability to engineer absorption by control of material properties or nanostructure geometry offers an opportunity to engineer absorptive resonances and thus realize selective thermal emission from the same surfaces when heated.[6,21,22] Though thermal emitters are extremely inefficient light sources (the incandescent light bulb being the most obvious example), at MIR wavelengths they provide reasonable power densities across a broad range of wavelengths, and are thus ubiquitous in IR spectroscopy. However, as Kirchoff's law states, the emissivity of a reciprocal medium is equal to the absorption, thus, through polaritonic resonator design, one can achieve narrow-band thermal emitters, rather than the broad-band response typically observed with incandescent light sources.

Spectral and angular control of polarized thermal emission was demonstrated in 2002 by Greffet et al. using a SiC surface that was patterned and etched into a periodic grating structure (Fig. 7a).[6] At wavelengths in the SiC Reststrahlen band, the negative permittivity of the material enabled propagating SPhPs to be supported at the SiC/air interface. Coupling from free space to the SPhP modes was achieved via the momentum matching provided by the etched grating, with the coupling wavelength dependent the grating period at a specific angle. Conversely, thermally excited SPhP modes are able to out-couple via the same mechanism. This resulted in a spatially coherent light

24

source with each of the SPhP frequencies emitted at a specific angle into free-space, dictated by the grating pitch (Fig. 7b). Strong, narrow and spatially coherent emission peaks were observed by the authors, via angular- and polarization-dependent FTIR emission and reflection spectroscopy, with the results matching well with the simulated response. While random thermal motion should generally result in incoherent thermal emission, the thermal excitation of a SPhP converts thermal energy into a delocalized collective and coherent oscillation, whose spatial coherence is sufficient to allow for far-field interference of photons out-coupled from the periodic grating structure. The demonstration of this coherent thermal emission came at an opportune time, with the fields of metamaterials, metasurfaces, plasmonics and phononics providing numerous examples of structures and materials with designable optical properties. In particular, due to the top-down nature of standard microelectronic fabrication processes, engineering the optical properties of surfaces or few-layer patterned thin films allowed for rather straightforward engineering of emissivity across the broad range of IR wavelengths.[54,117] Thermal emission from patterned metallic films, via out-coupling of surface 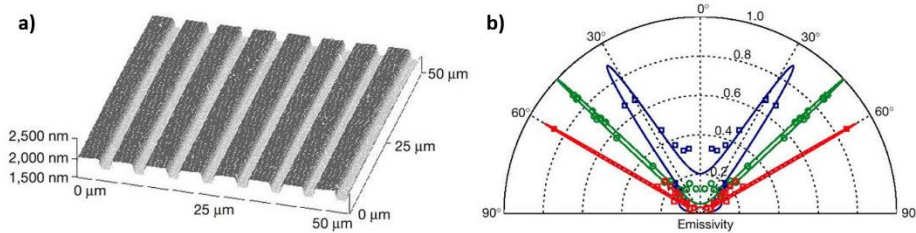waves on the metal/air interface have been demonstrated from periodic gratings,[6,67,118] bullseye structures,[119] and organ pipe resonators.[120]

As discussed in Section II, the propagating polariton requires momentum matching to couple to free space. This requirement allows for the highly directional nature of emission from periodically patterned surfaces,

Figure 7: a) AFM topographical plot of a SiC grating used to demonstrate spatially coherent thermal emission in the long-wave IR. The period was 0.55λ, with $\lambda=11.36$ µm. The ridges were etched to $\lambda/40$. b) Polar plot of the thermal emission spatial coherence at $\lambda=11.04$ (red), 11.36 (blue) and 11.86 µm. Experimental data extracted by specular reflectivity and applying Kirchoff's law are provided as the data points, while theoretical simulations are presented as the solid lines. Plots reproduced from Ref. 6.

as well as the ability to structure the far-field interference of scattered surface waves to form beaming or focusing structures.[119,121] The spatial dependence of thermal emission will vary significantly as a function of emission wavelength, such that the spatially integrated thermal emission from such a surface will be broadband in nature. Leveraging localized polaritons, however, allows for spectrally distinct, but largely angle-independent, coupling to free space light. The localized polariton analog of the patterned grating is the antenna, demonstrated initially in Ref. 21, which shows spectrally distinct emission peaks from a single SiC whisker antenna. These resonant peaks correspond to various antenna modes, even when thermal emission is collected by a high numerical aperture objective. Arrays of antenna structures, or metal-insulator-metal resonators, allow for control of surface emissivity over large areas,[22,70,122] with the thermal emission spectra controlled across the MIR and even into the FIR via choice of materials and resonator geometry.[69]

Recent efforts have explored the unique behavior associated with phononic and plasmonic materials at the LO phonon or plasma frequency, respectively, where the permittivity of the material approaches zero and the material behaves as an epsilon-near-zero, or ENZ, material. At the ENZ condition, the wavelength of a propagating mode in the material is dramatically extended, and a quasi-uniform phase is observed across distances larger than multiple free-space wavelengths.[56] A thin film of ENZ material is able to support a unique propagating mode, referred to as the Berreman mode,[51,52,123] which can be thought of as a hybrid EM/bulk excitation polaritonic mode.[51,52] Strong coupling to the Berreman mode can be observed in planar structures,[53,54,58] with momentum matching provided only by the incidence angle of the free-space light, though out-coupling via patterned structures is also possible.[124] Thermal emission from such layered structures is then monochromatic,[57] due to the narrow spectral band where the ENZ condition is fulfilled. Furthermore, the resonance frequency and linewidth can also be influenced further within planar films through implementation of strong coupling between SPPs and ENZ polaritons in adjacent bilayers.[53,59]

3. Exploring Mid- to Far-IR Polaritons via s-SNOM

Overall, s-SNOM has been used for many of the initial investigations of polaritonic systems, as it provides a tool that doesn't require significant processing of the sample being studied to directly measure propagating and/or localized polariton modes. This means that s-SNOM experiments do not directly study the properties of polaritonic devices usable for far-field optics, but instead provide invaluable information about electromagnetic near fields and materials properties. This has been demonstrated for chemical sensing,[116] on-chip photonic structures[125] and proposed for photonic circuits based on transformation optics.[126] Since its development, s-SNOM has been used for measuring polaritons in semiconductor and polar dielectrics.[2,10,28,93,95] However, while the initial studies provided significant insights into these polaritonic modes, including propagation lengths, field confinement and the ability to focus sub-diffractional modes,[96] it was following the discovery of graphene[127] that the application of this technique for characterization of polaritonic systems expanded dramatically. Within the basis of two-dimensional van der Waals materials and corresponding heterostructures,[128] a broad array of polaritons have been identified,[11] including exciton, Cooper-pair and magnon polaritons in addition to the previously discussed SPPs and SPhPs. For these 2D materials, the long-free space wavelengths coupled with the typically small-scale (microns to tens of microns) flakes that results from exfoliation from the bulk crystals, made characterization of polaritonic effects using conventional MIR spectroscopy difficult. The implementation of s-SNOM provided the means to overcome these limitations, providing direct imaging of polariton waves at the length scales commensurate with the deeply sub-diffractional compressed polariton wavelength, λ_{sp}.[41,129]

The implementation of s-SNOM in characterizing polaritonic effects within 2D materials was initiated by the seminal works of the Basov[41] and Koppens/Hillenbrand groups,[39] where SPPs within graphene were probed. While previously there had been theoretical studies of polariton dispersion within graphene[130] and experimental studies in

the far-field using nanoscale fabricated graphene resonators,[131] the works by these two groups for the first time directly imaged the SPP propagation within graphene. It should be noted that in later works,[98,125] additional so-called 'edge-launched' modes were observed due to direct launching of the polaritons from scattering of the incident light off of the flake edge. Surface polaritons have also been preferentially launched in 2D materials such as hBN via deposition of metallic pads on a portion of the flake, which in turn acts as the scattering site.[50,98]

In any of these approaches, the polariton decay rate and period can be extracted from the exponential decay of the oscillating s-SNOM amplitude as a function of distance from the flake edge. This can be used to determine the polariton propagation length and wavelength, and by extension, the carrier scattering rate and carrier concentration, following the approaches described earlier (Fig. 5a-d). From these highlighted works, SPP wavelengths were demonstrated as short as 260 nm, which is approximately 40x shorter than the free-space wavelength of the incident light at the same frequency.[39] Later efforts demonstrated wavelength compression in excess of 26,000x.[132] However, beyond providing a direct image of the SPP wave, the s-SNOM technique provides further diagnostic insights for polaritonic systems and devices. Specifically, for graphene and doped semiconductors, this polariton dispersion is directly dependent upon the Fermi energy. Essentially, with changing free carrier density, the slope of the dispersion changes, becoming steeper with increasing density due to the increased plasma frequency of the material.[48] By controlling the free carrier density *in situ*, one can extract the Fermi-energy dependent changes in the dispersion relationship, while also demonstrating the ability to actively tune the SPP response. This was demonstrated in those seminal works by Chen et al.[39] and Fei et al.[41] via electrostatic gating, however, in subsequent works this has also been demonstrated using optical pumping approaches.[103] More recently, cryogenic measurement schemes demonstrated the first observation of ballistic SPP propagation in graphene.[133]

4. **Far-IR tunable ENZ Modulator**s

Numerous demonstrations of passive SPhP-supporting structures often offer lower loss analogs of plasmonic phenomena, though at longer wavelengths (extending out to the far-IR for traditional III-V materials).[6,134] Ultimately, the creation of active IR devices is much more technologically significant. Currently there are extremely limited options for active modulation and control of MIR to FIR light, so the realization of such devices using polaritonic modes would be of immediate importance. The development of active SPhP-based devices, however, can be challenging, as they often require modulating relatively fixed quantities, such as the phonon energies or the geometry of the polaritonic material or structure, respectively. However, the total permittivity of a polar material will contain contributions from not only the phonon response, but also from the free carrier response and optical transitions between electronic states. Thus, the permittivity of a phononic material can be controlled by increasing the carrier density in the structure through the longitudinal optic phonon plasmon coupling (LOPC) effect,[31,32] modulating the carrier populations of bound states in a QW, and thus the contributions from intersubband transitions (ISBTs) to the dielectric tensor.

27

Leveraging the modulation from ISBTs requires a significant spatial overlap between the SPhP and the QW, which for a single interface SPhP is difficult, as the spatial extent of SPhPs is at least an order of magnitude larger than QW dimensions required for ISBTs at or near phonon energies.[135] To overcome the lack of overlap in traditional QW structures, the Greffet group took advantage of the ENZ polaritons within thin polar films.[51] An ISBT in an AlGaAs/GaAs QW between these interfaces is then used to electrically modulate the SPhP dispersion. Coupling to the ENZ mode is achieved using the grating approach discussed in previous sections, and the dynamic control of the near-ENZ permittivity via accumulation/depletion of the QW is observed by FTIR reflection spectroscopy from the grating-coupled device. This work demonstrated significant modulation of reflectance, evidence for active control of an optoelectronic device at the FIR phonon frequency of GaAs.

The experimental parameters in this example study demonstrate the significant challenges associated with FIR measurements of polaritonic structures and devices. As stated in the supplemental material of Ref. 136, scans were collected with the slowest FTIR scanner velocity and averaged over 512 scans, with each measurement taking over 3 hours. Considering the required single-beam reference spectrum for each sample spectrum and that a new sample spectra and reference spectra is needed for every reflectance curve, a substantial amount of time is invested into characterizing a single sample. Furthermore, if the device produces a significant amount of heat, long scan times could further obfuscate the measurement spectra.

The realization of active SPhP devices demonstrates the unique opportunities available for new classes of devices operating at FIR frequencies, where (relatively) small changes in carrier concentrations and the large oscillator strength of ISBTs can dramatically alter the permittivity of a material. While SPhPs are ultimately relegated to the rather narrow frequency range between or near the optic phonon frequencies, the hybridization of phononic, ISBT, and free carrier responses[48] does offer an opportunity to cover a broad range of FIR wavelengths with new classes of optoelectronic devices.

V. CONCLUSION/SUMMARY

In this tutorial we have provided an overview of the various techniques available for characterizing surface polaritons within the MIR to FIR. Specifically, we have detailed the methodology by which the polariton dispersion and dependence upon various material properties can be quantified. The increased complexities that result for such measurements in the MIR, and the increased complications that result in the FIR have been detailed, with the hope that this provides a more complete understanding for researchers entering this exciting area of science and engineering, thereby shortening the learning curve. The manner in which these various techniques have been implemented have been summarized for a few key examples, with the goal of providing direct context in how these approaches can be realized. In conclusion, it is the authors' hope that this tutorial can expand the basis of researchers working in this field and thus increase the potential for advanced technologies and new physical insights in the coming years.

28

ACKNOWLEDGEMENTS

REFERENCES

[1]   E.D. Palik, *Handbook of Optical Constants of Solids*. (Academic Press, Orlando, 1985);   P. Laporte, J.L. Subtil, M. Courbon, M. Bon, and L. Vincent, JOSA **73** (8), 1062 (1983);   Y. Nigara, JaJAP **7** (4), 404 (1968);   Y.-S. Jin, G.-J. Kim, and S.-G. Jeon, Journal of the Korean Physical Society **49** (2), 513 (2006).

[2]   A.J. Giles, S. Dai, I. Vurgaftman, A.J. Hoffman, S. Liu, L. Lindsay, C.T. Ellis, N. Assefa, I. Chatzakis, T.L. Reinecke, J.G. Tischler, M. M. Fogler, J.H. Edgar, D. N. Basov, and J.D. Caldwell, Nature Materials **17**, 134 (2018).

[3]   Joshua D Caldwell, Orest J Glembocki, Yan Francescato, Nicholas Sharac, Vincenzo Giannini, Francisco J Bezares, James P Long, Jeffrey C Owrutsky, Igor Vurgaftman, Joseph G Tischler, Virginia D Wheeler, Nabil D Bassim, Loretta M Shirey, Richard Kasica, and Stefan A Maier, Nano Lett. **13** (8), 3690 (2013).

[4]   E. Sachet, C.T. Shelton, J.S. Harris, B.E. Gaddy, D.L. Irving, S. Curtarolo, B.F. Donovan, P.E. Hopkins, P.A. Sharma, A.L. Sharma, J.F. Ihlefeld, S. Franzen, and J.P. Maria, Nature Materials **14**, 414 (2015).

[5]   Thomas G. Folland and Joshua D. Caldwell, in *Quantum Nano-Photonics*, edited by Baldassare Di Bartolo, Luciano Silvestri, Maura Cesaria et al. (Springer Netherlands, Dordrecht, 2018), pp. 235.

[6]   J.-J. Greffet, R. Carminati, K. Joulain, J.P. Mulet, S.P. Mainguy, and Y. Chen, Nature **416** (6876), 61 (2002).

[7]   M. Liu, A.J. Sternbach, and D. N. Basov, Rep. Prog. Phys. **80**, 014501 (2017).

[8]   T.G. Folland, T.W.W Maβ, J.R. Matson, J.R. Nolen, S. Liu, K. Watanabe, K. Taniguchi, J.H. Edgar, T. Taubner, and J.D. Caldwell, MRS Communications **8** (4), 1418 (2018).

[9]   T.W.W Maβ and T. Taubner, ACS Photonics **2**, 1498 (2015).

[10]   S. Dai, Z. Fei, Q. Ma, A.S. Rodin, M. Wagner, A.S. McLeod, M.K. Liu, W. Gannett, W. Regan, M. Thiemens, G. Dominguez, A.H. Castro Neto, A. Zettl, F. Keilmann, P. Jarillo-Herrero, M.M. Fogler, and D.N. Basov, Science (Wash.) **343** (6175), 1125 (2014).

[11]   D.N. Basov, M.M. Fogler, and F.J. Garcia de Abajo, Sci **354** (6309), aag1992 (2017);   T. Low, An. Chaves, J.D. Caldwell, A. Kumar, N.X. Fang, Ph. Avouris, T.F. Heinz, F. Guinea, L. Martin-Moreno, and F.H.L. Koppens, Nature Materials **16**, 182 (2017).

[12]   S.A. Maier, *Plasmonics: Fundamentals and Applications*. (Berlin, 2007).

[13]   N. Yu and F. Capasso, Nature Materials **13**, 139 (2014);   A.V. Kildishev, A. Boltasseva, and V.M. Shalaev, Science (Wash.) **339** (12), 1232009 (2013).

[14]   B. Neuner, D. Korobkin, C. Fietz, D. Carole, G. Ferro, and G. Shvets, Journal of Physical Chemistry C **114**, 7489 (2010); JD Caldwell, O Glembocki, FJ Bezares, ND Bassim, RW Rendell, M Feygelson, M Ukaegbu, R Kasica, L Shirey, and C Hosten, Acs Nano **5** (5), 4046 (2011); R. Adato, A.A. Yanik, J.J. Amsden, D.L. Kaplan, F.G. Omenetto, M.K. Hong, S. Erramilli, and H. Altug, Proc. Natl. Acad. Sci. USA **106** (46), 19227 (2009).

[15]   R. Berte, C.R. Gubbin, V.D. Wheeler, A.J. Giles, V. Giannini, S.A. Maier, S. De Liberato, and J.D. Caldwell, ACS Photonics **5** (7), 2807 (2017).

[16]   A. Neogi, C.-W. Lee, H.O. Everitt, T. Kuroda, A. Tackeuchi, and E. Yablonovitch, PhRvB **66**, 153305 (2002); E. Fort and S. Gresillon, JPhD **41**, 013001 (2007).

[17]   B. Song, Y. Ganjeh, S. Sadat, D. Thompson, A. Fiorino, V. Fernandez-Hurtado, J. Feist, F.J. Garcia-Vidal, J.C. Cuevas, P. Reddy, and E. Meyhofer, Nature Nanotechnology **10** (3), 253 (2015).

[18]   J.B. Khurgin and G. Sun, Appl. Phys. Lett. **96**, 181102 (2010);   J.B. Khurgin and G. Sun, Appl. Phys. Lett. **99**, 211106 (2011).

[19]   Justus C Ndukaife, Vladimir M. Shalaev, and Alexandra Boltasseva, Science **351** (6271), 334 (2016).

[20]   J.B. Khurgin and A. Boltasseva, MRS Bull. **37**, 768 (2012).

[21]   J.A. Schuller, T. Taubner, and M.L. Brongersma, Nature Photonics **3**, 658 (2009).

[22]   T. Wang, P. Li, D.N. Chigrin, A.J. Giles, F.J. Bezares, O.J. Glembocki, J.D. Caldwell, and T. Taubner, ACS Photonics **4** (7), 1753 (2017).

[23]   W.A. Challener, C. Peng, A.V. Itagi, D. Karns, W. Peng, Y. Peng, X. Yang, X.L. Zhu, N.J. Godkemeijer, Y.-T. Hsia, G. Ju, R.E. Rottmayer, M.A. Seigler, and E.C. Gage, Nature Photonics **3**, 220 (2009).

[24]   A. Gobin, M.H. Lee, N.J. Halas, J.W. Drezek, and J. West, Nano Lett. **7**, 1929 (2007).

25 O. Neumann, A.S. Urban, J. Day, S. Lal, P. Nordlander, and N.J. Halas, ACS Nano **7** (1), 42 (2013).

26 C.F. Bohren and D.R. Huffman, *Absorption and Scattering of Light by Small Particles*. (John Wiley & Sons, Inc., Weinheim, Germany, 2004).

27 J.D. Caldwell, L. Lindsey, V. Giannini, I. Vurgaftman, T. Reinecke, S.A. Maier, and O.J. Glembocki, Nanophotonics **4**, 44 (2015).

28 R. Hillenbrand, T. Taubner, and F. Keilmann, Nature **418** (6894), 159 (2002).

29 S. Law, D. C. Adams, A. M. Taylor, and D. Wasserman, Optics Express **20** (11), 12155 (2012).

30 S. Law, L. Yu, and D. Wasserman, J. Vac. Sci. Technol., B **31**, 03C121 (2013).

31 A.D. Dunkelberger, C.T. Ellis, D.C. Ratchford, A.J. Giles, M. Kim, C. Kim, B.T. Spann, I. Vurgaftman, J.G. Tischler, J.P. Long, O.J. Glembocki, J.C. Owrutsky, and J.D. Caldwell, Nature Photonics **12**, 50 (2018).

32 B.T. Spann, R. Compton, D.C. Ratchford, J.P. Long, A.D. Dunkelberger, P.B. Klein, A.J. Giles, J.D. Caldwell, and J.C. Owrutsky, PhRvB **93**, 085205 (2016).

33 N. Kinsey, C. DeVault, J. Kim, M. Ferrera, V. M. Shalaev, and A. Boltasseva, Optica **2** (7), 616 (2015).

34 M. Liu, X. Yin, E. Ulin-Avila, B. Geng, T. Zentgraf, L. Ju, F. Wang, and X. Zhang, Nature **474**, 64=67 (2011).

35 Dimitri Dini, Rüdeger Köhler, Alessandro Tredicucci, Giorgio Biasiol, and Lucia Sorba, Physical Review Letters **90** (11), 116401 (2003).

36 P. Hawrylak, J.-W. Wu, and J.J. Quinn, PhRvB **31**, 7855 (1985).

37 Stephanie Law, Runyu Liu, and Daniel Wasserman, Journal of Vacuum Science & Technology B **32** (5), 052601 (2014); K.P. Kelley, E. Sachet, C.T. Shelton, and J.P. Maria, APL Materials **5**, 076105 (2017); A. Boltasseva and H.A. Atwater, Science (Wash.) **331** (6015), 290 (2011).

38 S. Law, C. Roberts, T. Kilpatrick, L. Yu, T. Ribaudo, E. A Shaner, V. Podolskiy, and D. Wasserman, Physical Review Letters **112** (1), 017401 (2014).

39 J. Chen, M. Badioli, P. Alonso-Gonzalez, S. Thongrattanasiri, F. Huth, J. Osmond, M. Spasenovic, A. Centeno, A. Pesquera, P. Godignon, A.Z. Elorza, N. Camara, F.J. Garcia de Abajo, R. Hillenbrand, and F.H.L. Koppens, Nature **487**, 77 (2012).

40 S. Dai, Q. Ma, M. K. Liu, T. Andersen, Z. Fei, M. D. Goldflam, M. Wagner, K. Watanabe, T. Taniguchi, M. Thiemens, F. Keilmann, G. C. A. M. Janssen, S-E. Zhu, P. Jarillo-Herrero, M. M. Fogler, and D. N. Basov, Nature Nanotechnology **10**, 682 (2015).

41 Z. Fei, A.S. Rodin, G.O. Andreev, W. Bao, A.S. McLeod, M. Wagner, L.M. Zhang, Z. Zhao, M. Thiemens, G. Dominguez, M.M. Fogler, A.H. Castro Neto, C.N. Lau, F. Keilmann, and D.N. Basov, Nature **487**, 82 (2012).

42 M. Ferrera, N. Kinsey, A. Shaltout, C. DeVault, V.M. Shalaev, and A. Boltasseva, Journal of Optical Society America B **34** (1), 95 (2016); A. D. Dunkelberger, B. T. Spann, K. P. Fears, B. S. Simpkins, and J. C. Owrutsky, Nature Communications **7**, 13504 (2016).

43 S. Adachi, in *Optical Properties of Crystalline and Amorphous Semiconductors: Materials and Fundamental Principles* (Springer Science+Business Media, LLC, New York, NY, 1999), pp. 33.

44 P.Y. Yu and M. Cardona, *Fundamentals of Semiconductors: Physics and Materials Properties*. (Springer, New York, NY, 1999).

45 M.A. Stroscio and M. Dutta, *Phonons in Nanostructures*. (Cambridge University Press, 2001).

46 M. Scharte, R. Porath, T. Ohms, M. Aeschlimann, J.R. Krenn, H. Ditlbacher, F.R. Aussenegg, and A. Liebsch, Appl. Phys. B **73**, 305 (2001).

47 W. Ma, P. Alonso-Gonzalez, S. Li, A.Y. Nikitin, J. Yuan, J. Martin-Sanchez, J. Taboada-Gutierrez, I. Amenabar, P. Li, S. Velez, C. Tollan, Z. Dai, Y. Zhang, S. Sriram, K. Kalantar-Zadeh, Sh-T. Lee, R. Hillenbrand, and Q. Bao, Nature **562**, 557 (2018).

48 Joshua D. Caldwell, Igor Vurgaftman, Joseph G. Tischler, Orest J. Glembocki, Jeffrey C. Owrutsky, and Thomas L. Reinecke, Nature Nanotechnology **11**, 9 (2016).

49 H. Ma, C. Li, S. Tang, J. Yan, A. Alatas, L. Lindsay, B.C. Sales, and Z. Tian, PhRvB **94**, 220303(R) (2016).

50 E. Yoxall, M. Schnell, A.Y. Nikitin, O. Txoperena, A. Woessner, M.B. Lundeberg, F. Casanova, L.E. Hueso, F. H. L. Koppens, and R. Hillenbrand, Nature Photonics **9**, 674 (2015).

51 S. Campione, I. Brener, and F. Marquier, PhRvB **91**, 121408(R) (2015).

52 S. Vassant, J.-P. Hugonin, F. Marquier, and J.-J. Greffet, Opt. Express **20** (21), 23971 (2012).

53 N.C. Passler, C.R. Gubbin, T.G. Folland, I. Razdolski, D.S. Katzer, D.F. Storm, M. Wolf, S. De Liberato, J.D. Caldwell, and A. Paarmann, Nano Lett. **Articles ASAP**, DOI: 10.1021/acs.nanolett.8b01273 (2018).

54 K.P. Kelley, E.L. Runnerstrom, E. Sachet, E. Grimley, J. LeBeau, J.D. Caldwell, J. Levy, J. Suen, W.J. Padilla, and J.P. Maria, To be submitted (2017).

30

55 E.L. Runnerstrom, K.P. Kelley, E. Sachet, C.T. Shelton, and J.P. Maria, ACS Photonics **4** (8), 1885 (2017).

56 M.G. Silveirinha and N. Engheta, Phys. Rev. Lett. **97**, 157403 (2006).

57 L. Nordin, G. Dominguez, C.M. Roberts, W. Streyer, K. Feng, Z. Fang, V.A. Podolskiy, A.J. Hoffman, and D. Wasserman, Appl. Phys. Lett. **111**, 091105 (2017).

58 E.L. Runnerstrom, K.P. Kelley, E. Sachet, C.T. Shelton, and J.P. Maria, ACS Photonics **4**, 1885 (2017).

59 E.L. Runnerstrom, K.P. Kelley, T.G. Folland, J.R. Nolen, N. Engheta, J.D. Caldwell, and J.P. Maria, Nano Lett. **Article ASAP, DOI: 10.1021/acs.nanolett.8b04182** (2018).

60 H. Raether, *Surface plasmons on smooth and rough surfaces and on gratings*. (Springer-Verlag, Berlin ; New York, 1988), pp.x; Karsten Pufahl, Nikolai Christian Passler, Nicolai B. Grosse, Martin Wolf, Ulrike Woggon, and Alexander Paarmann, Applied Physics Letters **113** (16), 161103 (2018).

61 J.D. Caldwell, O.J. Glembocki, F.J. Bezares, M. Kariniemi, J. Niinisto, T. Hatanpaa, R.W. Rendell, M. Ukaegbu, M. Ritala, S.M. Prokes, C. Hosten, and M. Leskela, Opt. Express **19** (27), 26056 (2011).

62 J.D. Caldwell, A. Kretinin, Y. Chen, V. Giannini, M.M. Fogler, Y. Francescato, C. Ellis, J.G. Tischler, C. Woods, A.J. Giles, M. Hong, K. Watanabe, T. Taniguchi, S.A. Maier, and K.S. Novoselov, Nature Communications **5**, 5221 (2014).

63 Sarah M. Adams, Salvatore Campione, Joshua D. Caldwell, Francisco J. Bezares, James C. Culbertson, Filippo Capolino, and Regina Ragan, Small **8** (14), 2239 (2012); J.D. Caldwell, O.J. Glembocki, F.J. Bezares, N.D. Bassim, R.W. Rendell, M. Feygelson, M. Ukaegbu, R. Kasica, L. Shirey, and C. Hosten, ACS Nano **5** (5), 4046 (2010).

64 Werner Herres and Joern Gronholz, Part **1**, 352 (1984); Peter R. Griffiths, *Fourier Transform Infrared spectrometry*, 2nd Ed. ed. (Wiley-Interscience, Hoboken, N.J., 2007).

65 Antoni Rogalski, Infrared Physics & Technology **43** (3), 187 (2002).

66 D.C. Ratchford, P. Dev, N. Passler, I. Chatzakis, C. Winta, I. Razdolski, C. Ellis, J. Winterstein, J.G. Tischler, I. Vurgaftman, M. Katz, N. Nepal, T. Reinecke, A.J. Giles, D.S. Katzer, N.D. Bassim, R. Stroud, M. Wolf, A. Paarmann, and J.D. Caldwell, To be submitted (2017).

67 J.A. Mason, D.C. Adams, Z. Johnson, S. Smith, A.W. Davis, and D. Wasserman, Opt. Express **18**, 25192 (2010).

68 W. Streyer, S. Law, A. Rosenberg, C. Roberts, V.A. Podolskiy, A.J. Hoffman, and D. Wasserman, Appl. Phys. Lett. **104**, 131105 (2014).

69 S. Streyer, K. Feng, Y. Zhong, A.J. Hoffman, and D. Wasserman, Appl. Phys. Lett. **107**, 081105 (2015).

70 J.A. Mason, S. Smith, and D. Wasserman, Appl. Phys. Lett. **98**, 241105 (2011).

71 Y. Xiao, A. Shahsafi, C. Wan, P.J. Roney, G. Joe, Z. Yu, J. Salman, and M.A. Kats, arXiv: 1807.08682 (2018).

72 D. Kember, D.H. Chenery, N. Sheppard, and J. Fell, Spectrochim. Acta, Pt. A: Mol. Spectrosc. **35A**, 455 (1979).

73 R.J. Brown and B.G. Young, Appl. Opt. **14**, 2927 (1975).

74 P.R. Griffiths, Appl. Spectrosc. **26**, 73 (1972).

75 P.K. Gupta and S.C. Mehendale, Hyperfine Interact. **37**, 243 (1987).

76 B. Neuner, D. Korobkin, C. Fietz, D. Carole, G. Ferro, and G. Shvets, Opt. Lett. **34** (17), 2667 (2009).

77 N. Passler, I. Razdolski, S. Gewinner, W. Schollkopf, M. Wolf, and A. Paarmann, ACS Photonics **4** (5), 1048 (2017).

78 T. Inushima, K. Fukui, H. Lu, and W.J. Schaff, Appl. Phys. Lett. **92**, 171905 (2008).

79 J. Faist, F. Capasso, D.L. Sivco, C. Sirtori, A.L. Hutchinson, and A.Y. Cho, Sci **264**, 553 (1994); Y. Yao, A.J. Hoffman, and C.F. Gmachl, Nature Photonics **6**, 432 (2012).

80 R.Q. Yang, Superlattices Microstruct. **17**, 77 (1995); J.R. Meyer, I. Vurgaftman, R.Q. Yang, and L.R. Ram-Mohan, Electron. Lett **32**, 45 (1996); I. Vurgaftman, J.R. Meyer, and L.R. Ram-Mohan, IJQE **34**, 147 (1997); C.H. Lin, R.Q. Yang, D. Zhang, S.J. Murry, S.S. Pei, A.A. Allerman, and S.R. Kurtz, Electron. Lett **33**, 598 (1997); B.H. Yang, D. Zhang, R.Q. Yang, C.H. Lin, S.J. Murry, and S.S. Pei, Appl. Phys. Lett. **72**, 2220 (1998).

81 S. Herminjard, L. Sirigu, H.P. Herzig, E. Studemann, A. Crottini, J.-P. Pellaux, T. Gresch, M. Fischer, and J. Faist, Opt. Express **17** (1), 293 (2009).

82 T. Ribaudo, D.C. Adams, B. Passmore, E.A. Shaner, and D. Wasserman, Appl. Phys. Lett. **94**, 201109 (2009).

83 D.C. Adams, S. Thongrattanasiri, T. Ribaudo, V.A. Podolskiy, and D. Wasserman, Appl. Phys. Lett. **96**, 201112 (2010); S. Thongrattanasiri, D.C. Adams, D. Wasserman, and V.A. Podolskiy, Opt. Express **19**, 9269 (2011).

84 B.G. Lee, M.A. Belkin, C. Pflugl, L. Diehl, H.A. Zhang, R.M. Audet, J. MacArthur, D.P. Bour, S.W. Corzine, G.E. Hofler, and F. Capasso, IJQE **45** (5), 554 (2009); R. Maulini, D.A. Yarekha, J.-M. Bulliard, M. Giovannini, J. Faist, and E. Gini, Opt. Lett. **30** (19), 2584 (2005).

85 J.S. Sanghera, L.B. Shaw, and I.D. Aggarwal, IEEE Journal of Selected Topics in Quantum Electronics **15** (1), 114 (2009); S.D. Jackson, Nature Photonics **6**, 423 (2012).

86   C.R. Petersen, U. Moller, I. Kubat, B. Zhou, S. Dupont, J. Ramsay, T. Benson, S. Sujecki, N.A. Moneim, Z. Tang, D. Furniss, A. Seddon, and O. Bang, Nature Photonics **8**, 830 (2014).

87   I. Kubat, C.R. Petersen, U. Moller, A. Seddon, T. Benson, L. Brilland, D. Mechin, P.M. Moseland, and O. Bang, Opt. Express **22**, 3959 (2014); L.-R. Robichaud, V. Fortin, J.-C. Gauthier, S. Chatigny, J.-F. Couillard, J.-L. Delarosbil, R. Vallee, and M. Bernier, Opt. Lett. **41**, 4605 (2016).

88   N. Yu, R. Blanchard, J. Fan, T. Edamura, M. Yamanishi, H. Kan, and F. Capasso, Appl. Phys. Lett. **93**, 181101 (2008).

89   N. Yu, Q.J. Wang, C. Pflugl, L. Diehl, F. Capasso, T. Edamura, S. Furuta, M. Yamanishi, and H. Kan, Appl. Phys. Lett. **94**, 151101 (2008).

90   C. Sirtori, J. Faist, F. Capasso, D.L. Sivco, A.L. Hutchinson, and A.Y. Cho, Appl. Phys. Lett. **66**, 3242 (1995).

91   N. Ohtani, B. Meng, M. Franckie, L. Bosco, C. Ndebeka-Bandou, M. Beck, and J. Faist, Arxiv: 1808.09844 (2018); K. Ohtani, C. Ndebeka-Bandou, L. Bosco, M. Beck, and J. Faist, Arxiv **1610.00963** (2018).

92   F. Keilmann and R. Hillenbrand, in *Nano-Optics and Near-Field Optical Microscopy*, edited by A. Zayats and D. Richard (ArtechHouse, 2009), pp. 235.

93   A. Huber, N. Ocelic, D. Kazantsev, and R. Hillenbrand, Appl. Phys. Lett. **87**, 081103 (2005); N. Ocelic and R. Hillenbrand, Nature Materials **3**, 606 (2004).

94   S. Dai, Q. Ma, T. Anderson, A.S. McLeod, Z. Fei, M.K. Liu, M. Wagner, K. Watanabe, T. Taniguchi, M. Thiemens, F. Keilmann, P. Jarillo-Herrero, M.M. Fogler, and D.N. Basov, Nature Communications **6**, 6963 (2015); P. Li, M. Lewin, A.V. Kretinin, J.D. Caldwell, K.S. Novoselov, T. Taniguchi, K. Watanabe, F. Gaussmann, and T. Taubner, Nature Communications **6**, 7507 (2015); T. Taubner, D. Korobkin, Y. Urzhumov, G. Shvets, and R. Hillenbrand, Science (Wash.) **313**, 1595 (2006).

95   A.J. Giles, S. Dai, O.J. Glembocki, A.V. Kretinin, Z. Sun, C.T. Ellis, J.G. Tischler, T. Taniguchi, K. Watanabe, M.M. Fogler, K.S. Novoselov, D.N. Basov, and J.D. Caldwell, Nano Lett. **16** (6), 3858 (2016).

96   A.J. Huber, B. Deutsch, L. Novotny, and R. Hillenbrand, Appl. Phys. Lett. **92**, 203104 (2008).

97   S. Dai, Q. Ma, M.K. Liu, T. Anderson, Z. Fei, M.D. Goldflam, M. Wagner, K. Watanabe, T. Taniguchi, M. Thiemens, F. Keilmann, G.C.A.M. Janssen, S.-E. Zhu, P. Jarillo-Herrero, M. M. Fogler, and D. N. Basov, Nature Nanotechnology **10**, 682 (2015); G.X. Xu, B.G. Ghamsari, J-H. Jiang, L. Gilburd, G.O. Andreev, C. Zhi, Y. Bando, D. Golberg, P. Berini, and G.C. Walker, Nature Communications **5**, 4782 (2014); X.G. Xu, A.E. Tanur, and G.C. Walker, J. Phys. Chem. A **117**, 3348 (2013).

98   S. Dai, Q. Ma, Y. Yang, J. Rosenfeld, M.D. Goldflam, A.S. McLeod, Z. Sun, T.I. Andersen, Z. Fei, M. Liu, Y. Shao, K. Watanabe, K. Taniguchi, M. Thiemens, F. Keilmann, P. Jarillo-Herrero, M. M. Fogler, and D. N. Basov, Nano Lett. **17** (9), 5285 (2017).

99   S. Dai, M. Tymchenko, Z.-Q. Xu, T.T. Tran, Y. Yan, Q. Ma, K. Watanabe, K. Taniguchi, P. Jarillo-Herrero, I. Aharonovich, D. N. Basov, T.H. Tao, and A. Alu, Nano Lett. **18** (8), 5205 (2018).

100 B. Hauer, C.E. Marvinney, M. Lewin, N. A. Mahadik, J. K. Hite, N.D. Bassim, A. J. Giles, R. E. Stahlbush, J. D. Caldwell, and T. Taubner, To be submitted (2019).

101 F. Huth, A. Govyadinov, S. Amarie, W. Nuansing, F. Keilmann, and R. Hillenbrand, Nano Lett. **12**, 3973 (2012); S. Amarie and F. Keilmann, PhRvB **83**, 045404 (2011).

102 G.X. Ni., L. Wang, M.D. Goldflam, M. Wagner, Z. Fei, A.S. McLeod, M.K. Liu, F. Keilmann, B. Ozyilmaz, A.H. Castro Neto, J. Hone, M. M. Fogler, and D. N. Basov, Nature Photonics **10**, 244 (2016).

103 M. Wagner, Z. Fei, A.S. McLeod, A.S. Rodin, W. Bao, E.G. Iwinski, Z. Zhao, M.D. Goldflam, M.K. Liu, G. Dominguez, M. Thiemens, M. M. Fogler, A.H. Castro Neto, C.N. Lau, S. Amarie, F. Keilmann, and D. N. Basov, Nano Lett. **14** (2), 894 (2014).

104 M. Liu, A.J. Sternbach, and D. N. Basov, Rep. Prog. Phys. **80**, 27 (2017).

105 H.A. Bechtel, E.A. Muller, R.L. Olmon, M.C. Martin, and M.B. Raschke, PNAS **111** (20), 7191 (2014).

106 L.V. Brown, M. Davanco, Z. Sun, A. Kretinin, Y. Chen, J.R. Matson, I. Vurgaftman, N. Sharac, A. J. Giles, M.M. Fogler, T. Taniguchi, K. Watanabe, K.S. Novoselov, S. A. Maier, A. Centrone, and J. D. Caldwell, Nano Lett. **18** (3), 1628 (2018).

107 A. Centrone, Annual Review of Analytical Chemistry **8**, 101 (2015); A.M. Katzenmeyer, V. Aksyuk, and A. Centrone, Anal. Chem. **85** (4), 1972 (2013); A.M. Katzenmeyer, G. Holland, K. Kjoller, and A. Centrone, Anal. Chem. (Wash.) **87** (6), 3154 (2015); B. Lahiri, G. Holland, V. Aksyuk, and A. Centrone, Nano Lett. **13** (7), 3218 (2013).

108 A. Ambrosio, L.A. Jauregui, S. Dai, K. Chaudhary, M. Tamagnone, M. M. Fogler, D. N. Basov, F. Capasso, P. Kim, and W.L. Wilson, ACS Nano **11** (9), 8741 (2017).

32

109 A. Paarmann, I. Razdolski, S. Gewinner, W. Schollkopf, and M. Wolf, PhRvB **94**, 134312 (2016); I. Razdolski, Y. Chen, A.J. Giles, S. Gewinner, W. Schollkopf, M. Hong, M. Wolf, V. Giannini, J.D. Caldwell, S.A. Maier, and A. Paarmann, Nano Lett. **16**, 6954 (2016).

110 E.V. Loewenstein and D.R. Smith, Appl. Opt. **10**, 577 (1971).

111 Stephanie Law, Lan Yu, Aaron Rosenberg, and Daniel Wasserman, Nano Letters **13** (9), 4569 (2013).

112 Y. Chen, Y. Francescato, J.D. Caldwell, V. Giannini, T.W.W. Maß, O.J. Glembocki, F.J. Bezares, T. Taubner, R. Kasica, M. Hong, and S.A. Maier, ACS Photonics **1** (8), 718 (2014).

113 C.T. Ellis, J.G. Tischler, O.J. Glembocki, F.J. Bezares, A.J. Giles, R. Kasica, L. Shirey, J.C. Owrutsky, D.N. Chigrin, and J.D. Caldwell, Scientific Reports **6**, 32959 (2016).

114 T. E. Tiwald, J.A. Woolam, S. Zollner, J. Christiansen, R.B. Gregory, T. Wetteroth, S.R. Wilson, and A.R. Powell, PhRvB **60** (16), 11464 (1999).

115 T. Wang, P. Li, B. Hauer, D.N. Chigrin, and T. Taubner, Nano Lett. **13** (11), 5051 (2013).

116 M. Autore, P. Li, I. Dolado, F.J. Alfaro-Mozaz, R. Esteban, A. Atxabal, F. Casanova, L.E. Hueso, P. Alonso-Gonzalez, J. Aizpurua, A.Y. Nikitin, S. Velez, and R. Hillenbrand, Light: Science & Applications **doi: 10.1038/lsa.2017.172** (2017).

117 J.A. Mason, D.C. Adams, Z. Johnson, S. Smith, A.W. Davis, and D. Wasserman, Opt. Express **18**, 25192 (2010).

118 F. Marquier, C. Arnold, M. Laroche, J.-J. Greffet, and Y. Chen, Opt. Express **16** (8), 5305 (2008); M. Kreiter, J. Oster, R. Sambles, S. Herminghaus, S. Mittler-Neher, and W. Knoll, Opt. Commun. **168** (1-4), 117 (1999); J.T.K. Wan, Opt. Commun. **282** (8), 1671 (2009).

119 S.E. Han and D.J. Norris, Opt. Express **18**, 4829 (2010).

120 K. Ikeda, H.T. Miyazaki, T. Kasaya, Y. Yamamoto, Y. Inoue, K. Fujimura, T. Kanakugi, M. Okada, K. Hatade, and S. Kitagawa, Appl. Phys. Lett. **92** (2), 021117 (2008); H.T. Miyazaki, K. Ikeda, T. Kasaya, Y. Yamamoto, Y. Inoue, K. Fujimura, T. Kanakugi, M. Okada, K. Hatade, and S. Kitagawa, Appl. Phys. Lett. **92** (14), 141114 (2008).

121 H. Chalabi, A. Alu, and M.L. Brongersma, PhRvB **94**, 094307 (2016).

122 X. Liu, T. Tyler, T. Starr, A.F. Starr, N.M. Jokerst, and W.J. Padilla, Phys. Rev. Lett. **107**, 045901 (2011).

123 B. Harbecke, B. Heinz, and P. Grosse, Appl. Phys. A **38**, 263 (1985).

124 B. Askenazi, A. Vasanelli, Y. Todorov, E. Sakat, J.-J. Greffet, G. Beaudoin, I. Sagnes, and C. Sirtori, ACS Photonics **4**, 2550 (2017).

125 T.G. Folland, A. Fali, S.T. White, J.R. Matson, S. Liu, N.A. Aghamiri, J.H. Edgar, R.F. Haglund, Y. Abate, and J.D. Caldwell, Nature Communications **9**, 4371 (2018).

126 N. Engheta, Science (Wash.) **317**, 1698 (2007); N. Engheta, PhyW **23**, 31 (2010).

127 K.S. Novoselov, A.K. Geim, S.V. Morozkov, D.A. Jiang, Y. Zhang, S.V. Dubonos, I.V. Grigorieva, and A.A. Firsov, Sci **306** (5696), 666 (2004); Y. Zhang, Y.-W. Tan, H.L. Stormer, and P. Kim, Nature **438**, 201 (2005); K.S. Novoselov, A.K. Geim, S.V. Morozkov, D.A. Jiang, M.I. Katsnelson, I.V. Grigorieva, S.V. Dubonos, and A.A. Firsov, Nature **438**, 197 (2005).

128 A.K. Geim and I.V. Grigorieva, Nature **499**, 419 (2013).

129 J. N. Chen, M. Badioli, P. Alonso-Gonzalez, S. Thongrattanasiri, F. Huth, J. Osmond, M. Spasenovic, A. Centeno, A. Pesquera, P. Godignon, A. Z. Elorza, N. Camara, F. J. G. de Abajo, R. Hillenbrand, and F. H. L. Koppens, Nature **487** (7405), 77 (2012).

130 M. Jablan, H. Buljan, and M. Soljacic, PhRvB **80**, 245435 (2009).

131 H. Yan, T. Low, W. Zhu, Y. Wu, M. Freitag, X. Li, F. Guinea, Ph. Avouris, and F. Xia, Nature Photonics **7**, 394 (2013).

132 David Alcaraz Iranzo, Sébastien Nanot, Eduardo J. C. Dias, Itai Epstein, Cheng Peng, Dmitri K. Efetov, Mark B. Lundeberg, Romain Parret, Johann Osmond, Jin-Yong Hong, Jing Kong, Dirk R. Englund, Nuno M. R. Peres, and Frank H. L. Koppens, Science **360** (6386), 291 (2018).

133 G.X. Ni, A.S. McLeod, S. Zun, L. Wang, L. Xiong, K.W. Post, S.S. Sunku, B.Y. Jiang, J. Hone, C.R. Dean, M. M. Fogler, and D. N. Basov, Nature **557** (7706), 530 (2018).

134 J. Le Gall, M. Olivier, and J.-J. Greffet, PhRvB **55** (15), 10105 (1997).

135 A.V. Shchegrov, K. Joulain, R. Carminati, and J.-J. Greffet, Phys. Rev. Lett. **85**, 1548 (2000).

136 S. Vassant, A. Archambault, F. Marquier, F. Pardo, U. Gennser, A. Cavanna, J.L. Pelouard, and J.-J. Greffet, Phys. Rev. Lett. **109**, 237401 (2012).

33